

Y3. N 21/5:6/3348

GOVT. DOC.

NACA TN 3348

NATIONAL ADVISORY COMMITTEE FOR AERONAUTICS

BUSINESS AND
TECHNICAL DEPT.

TECHNICAL NOTE 3348

Dec 9 '54

A SYSTEM FOR MEASURING THE DYNAMIC LATERAL STABILITY
DERIVATIVES IN HIGH-SPEED WIND TUNNELS

By Henry C. Lessing, Thomas B. Fryer,
and Merrill H. Mead

Ames Aeronautical Laboratory
Moffett Field, Calif.



Washington

December 1954

TECHNICAL NOTE 3348

A SYSTEM FOR MEASURING THE DYNAMIC LATERAL STABILITY

DERIVATIVES IN HIGH-SPEED WIND TUNNELS

By Henry C. Lessing, Thomas B. Fryer,
and Merrill H. Mead

SUMMARY

A two-degree-of-freedom system, in which rolling oscillations are forced, is described. Details of the system, the theory, and the method of operation are discussed. It is shown that, although the system is characterized by nonlinear equations of motion, linearization of the equations by assuming small perturbations and constant coefficients yields sufficiently accurate results.

The accuracy of the system was first investigated in tests under idealized conditions in which the aerodynamic derivatives were simulated by the action of gyroscopes and magnetic dampers. Later, the system was investigated in a high-speed wind tunnel using a simple model for which the aerodynamic derivatives could be estimated.

The results of the tests showed that the quantities relating to the primary mode of operation of the system, that is, the rolling velocity derivatives, could be obtained satisfactorily. The same is true of the directional stability and the damping-in-yaw derivatives. Results obtained from the data-reduction equations for the rolling moment due to yawing velocity and due to sideslip angle were unreliable, however, and prevented the evaluation of these derivatives.

INTRODUCTION

The increasing emphasis placed on studies of the dynamic stability of aircraft has intensified the need for satisfactory methods for predicting the dynamic stability derivatives. Most theoretical methods evolved to date are subject to limitations imposed to reduce the mathematical task to reasonable proportions. In order to obtain experimental checks of these methods and to provide sources of information in those areas in which theoretical methods are not yet available, there exists a need for experimental research on the stability derivatives.

The experimental study of dynamic stability derivatives in wind tunnels is, of course, not new. Many systems have been evolved for this purpose. References 1, 2, and 3, for instance, discuss early British

systems in which the relative motion of the model and the air stream is generated by model motion. A dynamic system recently developed at Ames Aeronautical Laboratory is described in reference 4; again the relative motion of the model and the air stream is generated by model motion. The rolling- and curved-flow wind tunnels now in use at the Langley Aeronautical Laboratory of the NACA, for instance (refs. 5 and 6), are examples of other systems in which the model is held rigidly and the air flow generates the relative steady yawing and rolling motion..

In the present case, a system in which the model executes forced oscillations with two degrees of freedom was developed. The details of its design and development are published herewith since they may prove useful to others who desire to develop dynamic systems.

SYMBOLS AND COEFFICIENTS

The aerodynamic coefficients defined herein are referred to the system of body axes originating at the model center of gravity. The symbols and coefficients are defined as follows:

b body length, ft

$$C_{l_p} \quad L \dot{\phi} \left(\frac{2V}{qSb^2} \right)$$

$$C_{l_r} \quad L \dot{\psi} \left(\frac{2V}{qSb^2} \right)$$

$$C_{l_\beta} \quad L \beta \left(\frac{1}{qSb} \right)$$

$$C_{l_{\dot{\beta}}} \quad L \dot{\beta} \left(\frac{2V}{qSb^2} \right)$$

$$C_{n_p} \quad N \dot{\phi} \left(\frac{2V}{qSb^2} \right)$$

$$C_{n_r} \quad N \dot{\psi} \left(\frac{2V}{qSb^2} \right)$$

$$C_{n_\beta} \quad N \beta \left(\frac{1}{qSb} \right)$$

$$C_{n_{\dot{\beta}}} \quad N \dot{\beta} \left(\frac{2V}{qSb^2} \right)$$

f frequency, cps

H_X, H_Y, H_Z	moment of momentum about space-fixed axes
h_X, h_Y, h_Z	moment of momentum about body axes
I_X	moment of inertia about x axis, ft-lb sec ²
I_Z	moment of inertia about z axis, ft-lb sec ²
I_{XZ}	product of inertia with respect to x and z axes, ft-lb sec ²
I_{YZ}	product of inertia with respect to y and z axes, ft-lb sec ²
L	rolling moment, ft-lb
L_ϕ	absolute value of spring constant of roll flexure pivots, ft-lb/radian
$L\dot{\phi}$	rate of change of aerodynamic rolling moment with rolling angular velocity, ft-lb/radian/sec
$L\dot{\phi}_s$	equivalent viscous damping factor due to internal friction in roll flexure pivots, ft-lb/radian/sec
$L\dot{\psi}$	rate of change of aerodynamic rolling moment with yawing angular velocity, ft-lb/radian/sec
L_β	rate of change of rolling moment with sideslip angle, ft-lb/radian
$L\dot{\beta}$	rate of change of rolling moment per unit rate of change of sideslip angle, ft-lb/radian/sec
M	pitching moment, ft-lb
M_X, M_Y, M_Z	applied moments about space-fixed axes, ft-lb
N	yawing moment, ft-lb
N_ϕ	rate of change of aerodynamic yawing moment with rolling angular velocity, ft-lb/radian/sec
N_ψ	absolute value of spring constant of yaw flexure pivots, ft-lb/radian
$N\dot{\psi}$	rate of change of aerodynamic yawing moment with yawing angular velocity, ft-lb/radian/sec
$N\dot{\psi}_s$	equivalent viscous damping factor due to internal friction in yaw flexure pivots, ft-lb/radian/sec
N_β	rate of change of yawing moment with sideslip angle, ft-lb/radian

$N\dot{\beta}$	rate of change of yawing moment per unit rate of change of sideslip angle, ft-lb/radian/sec
$\dot{\phi}$	rolling angular velocity, radians/sec
q	dynamic pressure, lb/sq ft, $\frac{1}{2}\rho V^2$
r	maximum body radius, ft
$\dot{\psi}$	yawing angular velocity, radians/sec
S	maximum cross-sectional area of body, sq ft
T	roll input torque, ft-lb
t	time, sec
V	free-stream velocity, ft/sec
X, Y, Z	space-fixed axes
x, y, z	axes fixed with respect to the model (body axes)
α	angle of attack, radians
α_1	angle between free-stream velocity and longitudinal axis of support housing
β	angle of sideslip, radians
ϕ	angle of roll, radians
ψ	angle of yaw, radians
ϵ	phase angle between roll and yaw angles, positive for yaw leading roll, deg
Δ	phase angle between roll angle and roll-input torque, positive for input torque leading roll, deg
ω	angular frequency, $2\pi f$, radians/sec
ρ	mass density of air, slugs/cu ft
$()_o$	amplitude of oscillation or out-of-phase component
$()_i$	initial condition or in-phase component
$(\dot{\ })$	$\frac{d()}{dt}$

ANALYSIS AND DESCRIPTION

Coordinate System

The coordinate system for which the equations of motion will be written is shown in figure 1. The x,y,z axes are fixed with respect to the model and are therefore body axes. The X,Y,Z axes are aligned with the equilibrium position of the model and remain fixed in space.

In order to illustrate the possible modes of motion of the model, a schematic drawing of the mechanical apparatus is shown in figure 2(a). As shown in this diagram, the main shaft (torque tube) of the apparatus is driven in a constant-amplitude oscillatory rotation about the X axis which is transmitted directly to the model. The axis of rotation of the torque tube is defined by the roll flexure pivots and ball bearing which support the tube within the support housing. Attachment of the model to the torque tube is through the yaw flexure pivots which allow the model a second mode of motion, that of angular rotation about the z axis.

Equations of Motion

In accordance with the Newtonian laws of motion, the time rate of change of the moment of momentum about axes fixed in space is equal to the summation of the externally applied moments about those axes:

$$\left. \begin{aligned} \Sigma M_X &= \frac{dH_X}{dt} \\ \Sigma M_Y &= \frac{dH_Y}{dt} \\ \Sigma M_Z &= \frac{dH_Z}{dt} \end{aligned} \right\} \quad (1)$$

Since the model is rigidly constrained in pitch, the second of equations (1) need not be considered.

The time rate of change of the moments of momentum about fixed-space axes in terms of the rate of change about the body axis system may be written (see, i.e., ref. 7):

$$\left. \begin{aligned} \frac{dH_X}{dt} &= \frac{dh_X}{dt} - h_y \dot{\psi} \\ \frac{dH_Z}{dt} &= \frac{dh_Z}{dt} + h_y \dot{\phi} \end{aligned} \right\} \quad (2)$$

where

$$\left. \begin{aligned} h_x &= \dot{\phi} I_{IX} + \dot{\psi} I_{IXZ} \\ h_y &= -\dot{\phi} I_{IXY} - \dot{\psi} I_{IYZ} \\ h_z &= \dot{\phi} I_{IXZ} + \dot{\psi} I_{IZ} \end{aligned} \right\} \quad (3)$$

The applied moments and inertial reactions can then be expressed in terms of the body axis variables

$$\left. \begin{aligned} \Sigma L &= I_X \ddot{\phi} + I_{XZ} \ddot{\psi} + I_{XY} \dot{\psi} \dot{\phi} + I_{YZ} \dot{\psi}^2 \\ \Sigma N &= I_Z \ddot{\psi} + I_{XZ} \ddot{\phi} - I_{XY} \dot{\phi}^2 - I_{YZ} \dot{\phi} \dot{\psi} \end{aligned} \right\} \quad (4)$$

Substituting the externally applied moments for the left-hand side of equations (4) gives

$$\left. \begin{aligned} T \cos \psi + L_{\dot{\phi}_S} \dot{\phi} \cos \psi + L_{\phi} \dot{\phi} \cos \psi - L_{\dot{\phi}} \dot{\phi} + L_{\dot{\psi}} \dot{\psi} + L_{\dot{\beta}} \dot{\beta} + L_{\beta} \beta \\ = I_X \ddot{\phi} + I_{XZ} \ddot{\psi} + (I_{XY} \dot{\phi} \dot{\psi} + I_{YZ} \dot{\psi}^2) \\ N_{\dot{\psi}_S} \dot{\psi} + N_{\psi} \dot{\psi} + N_{\dot{\phi}} \dot{\phi} - N_{\dot{\psi}} \dot{\psi} + N_{\dot{\beta}} \dot{\beta} + N_{\beta} \beta = I_Z \ddot{\psi} + I_{XZ} \ddot{\phi} + (-I_{XY} \dot{\phi}^2 - I_{YZ} \dot{\phi} \dot{\psi}) \end{aligned} \right\} \quad (5)$$

A geometrical relationship exists between the angle of sideslip β and the roll and yaw angles ϕ and ψ as follows: Let the angle between the free-stream velocity and the X axis be α_1 .

From sketch (a),

$$w = V \sin \alpha_1 \quad V_1 = V \cos \alpha_1$$

and from sketch (b),

$$v = w \sin \phi = V \sin \alpha_1 \sin \phi$$

From sketch (c),

$$v_1 = v \cos \psi = V \sin \alpha_1 \sin \phi \cos \psi$$

$$v_2 = V_1 \sin \psi = V \cos \alpha_1 \sin \psi$$

The angle of sideslip is then given by

$$\beta = \sin^{-1} \left(\frac{v_1 - v_2}{V} \right)$$

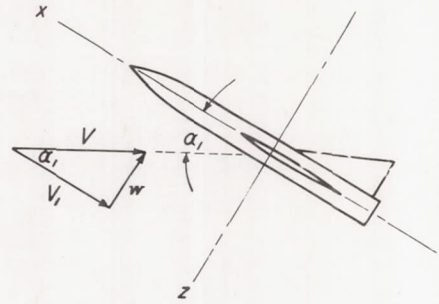
$$\beta = \sin^{-1} (\sin \alpha_1 \sin \phi \cos \psi - \cos \alpha_1 \sin \psi) \quad (6)$$

The true angle of attack is also a function of the roll angle:

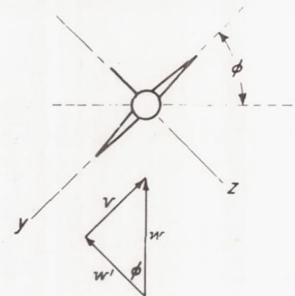
$$\begin{aligned} \alpha &= \sin^{-1} \frac{w'}{V} = \sin^{-1} \left(\frac{w \cos \phi}{V} \right) \\ &= \sin^{-1} (\sin \alpha_1 \cos \phi) \end{aligned} \quad (7)$$

Substitution of equation (6) and its time rate of change in equations (5) yields the equations of motion, and it can be seen that nonlinear terms will appear both in the aerodynamic moments and the inertial reactions.

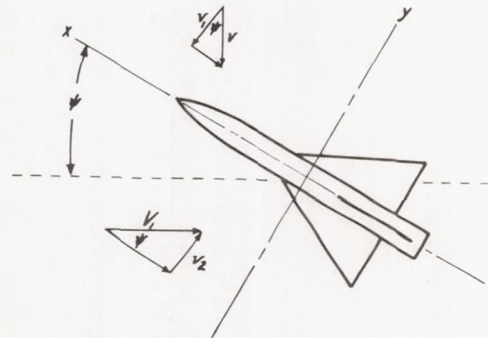
In order that they be of practical value for use with experimental wind-tunnel data, linearization of the equations is necessary. If the approximation is made that



Sketch (a)



Sketch (b)



Sketch (c)

$$\sin \phi = \phi \quad \sin \psi = \psi$$

$$\cos \phi = \cos \psi = 1$$

then the angle of attack becomes $\alpha = \alpha_1$, and the sideslip angle is given by

$$\beta = \phi \sin \alpha - \psi \cos \alpha \quad (8)$$

In general, the angle of attack is sufficiently small so that equation (8) may be written as

$$\beta = \alpha \phi - \psi \quad (9)$$

and the time rate of change of sideslip angle is given by

$$\dot{\beta} = \alpha \dot{\phi} - \dot{\psi} \quad (10)$$

For large angles of attack for which these approximations are not valid, equation (8) and its time derivative may be used.

If, in addition to the approximations made in equations (9) and (10), the second-order inertial terms in equations (5) are neglected, the equations of motion may be written

$$\left. \begin{aligned} T + (L\dot{\phi}_s + L\dot{\phi} + \alpha L\dot{\beta})\dot{\phi} - (L\phi - \alpha L\beta)\phi + (L\dot{\psi} - L\dot{\beta})\dot{\psi} - L\beta\psi &= I_x \ddot{\phi} + I_{xz} \ddot{\psi} \\ (N\dot{\phi} + \alpha N\dot{\beta})\dot{\phi} + \alpha N\beta\phi + (N\dot{\psi}_s + N\dot{\psi} - N\dot{\beta})\dot{\psi} - (N\psi + N\beta)\psi &= I_z \ddot{\psi} + I_{xz} \ddot{\phi} \end{aligned} \right\} (11)$$

The question immediately arises as to the accuracy with which equations (11) represent the physical system. In order to answer this question, transient solutions of both the nonlinear and linearized equations of motion for a pulse-type roll disturbance T were obtained on the Reeves Electronic Analog Computer for conditions expected to be encountered in wind-tunnel operation. Comparison of the solutions showed that the only discernible effect of linearization was a negligible difference in the roll and yaw accelerations. From this result it was concluded that the use of equations (11) would be a justifiable approximation, and that their use would yield data of sufficient accuracy. Further experimental verification of the validity of these equations is given in a later section.

Solution of Equations of Motion

In the following development the solution of the equations of motion will be given and arranged in a manner which will permit the determination of the desired aerodynamic parameters in terms of measured quantities.

Yaw equation.— The second of equations (11) may be rearranged and written

$$I_Z \ddot{\Psi} - (N_{\dot{\Psi}_S} + N_{\dot{\Psi}} - N_{\dot{\beta}}) \dot{\Psi} + (N_{\Psi} + N_{\beta}) \Psi = - I_{XZ} \ddot{\Phi} + (N_{\dot{\Phi}} + \alpha N_{\dot{\beta}}) \dot{\Phi} + \alpha N_{\beta} \Phi \quad (12)$$

Equation (12) is a linear second-order differential equation, the solution for which is well known. The roll angle ϕ is forced to vary harmonically with time; $\Phi = \Phi_0 \sin \omega t$. Then the solution, in general, consists of two parts: first, the complementary function, uniquely determined by the initial yaw angle Ψ and the initial yawing velocity $\dot{\Psi}$; and second, the particular integral, sometimes called the steady-state or frequency response, which is independent of the initial conditions, and is determined only by the applied disturbance, the right-hand side of equation (12).

The amplitude ratio and phase angle given by the particular integral are,

$$\frac{\Psi_0}{\Phi_0} = \sqrt{\frac{(\alpha N_{\beta} + I_{XZ} \omega^2)^2 + (N_{\dot{\Phi}} + \alpha N_{\dot{\beta}})^2 \omega^2}{(N_{\Psi} + N_{\beta} - I_Z \omega^2)^2 + (N_{\dot{\Psi}_S} + N_{\dot{\Psi}} - N_{\dot{\beta}})^2 \omega^2}} \quad (13)$$

$$\epsilon = \tan^{-1} \frac{(N_{\dot{\Phi}} + \alpha N_{\dot{\beta}}) \omega}{\alpha N_{\beta} + I_{XZ} \omega^2} + \tan^{-1} \frac{(N_{\dot{\Psi}_S} + N_{\dot{\Psi}} - N_{\dot{\beta}}) \omega}{(N_{\Psi} + N_{\beta}) - I_Z \omega^2} \quad (14)$$

Equation (14) may be manipulated to give

$$\alpha N_{\beta} + I_{XZ} \omega^2 = \frac{\omega (N_{\dot{\Phi}} + \alpha N_{\dot{\beta}}) [(N_{\Psi} + N_{\beta} - I_Z \omega^2) \cos \epsilon + (N_{\dot{\Psi}_S} + N_{\dot{\Psi}} - N_{\dot{\beta}}) \omega \sin \epsilon]}{(N_{\Psi} + N_{\beta} - I_Z \omega^2) \sin \epsilon - (N_{\dot{\Psi}_S} + N_{\dot{\Psi}} - N_{\dot{\beta}}) \omega \cos \epsilon}$$

$$(N_{\dot{\Phi}} + \alpha N_{\dot{\beta}}) \omega = \frac{(\alpha N_{\beta} + I_{XZ} \omega^2) [(N_{\Psi} + N_{\beta} - I_Z \omega^2) \sin \epsilon - (N_{\dot{\Psi}_S} + N_{\dot{\Psi}} - N_{\dot{\beta}}) \omega \cos \epsilon]}{(N_{\Psi} + N_{\beta} - I_Z \omega^2) \cos \epsilon + (N_{\dot{\Psi}_S} + N_{\dot{\Psi}} - N_{\dot{\beta}}) \omega \sin \epsilon}$$

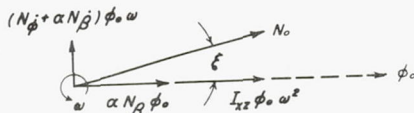
Substitution of these equations into equation (13) leads to two fundamental relationships:

$$\frac{\psi_0}{\phi_0} = \frac{(N_{\dot{\phi}} + \alpha N_{\dot{\beta}})\omega}{(N_{\psi} + N_{\beta} - I_z \omega^2) \sin \epsilon - (N_{\dot{\psi}_s} + N_{\dot{\psi}} - N_{\dot{\beta}})\omega \cos \epsilon} \quad (15)$$

$$\frac{\psi_0}{\phi_0} = \frac{\alpha N_{\beta} + I_{xz} \omega^2}{(N_{\psi} + N_{\beta} - I_z \omega^2) \cos \epsilon + (N_{\dot{\psi}_s} + N_{\dot{\psi}} - N_{\dot{\beta}})\omega \sin \epsilon} \quad (16)$$

The geometrical meaning of equations (15) and (16) is apparent from the concept of the rotating vector diagram (see, e.g., ref. 8). Since ϕ is a harmonically varying function $\phi = \phi_0 \sin \omega t$, the right-hand side of equation (12) represents a harmonically varying yawing moment N_0 with components proportional to the roll position, velocity, and acceleration. The vector diagram is shown in sketch (d). The magnitude of the

resulting yawing moment is



$$N_0 = \phi_0 \sqrt{(\alpha N_{\beta} + I_{xz} \omega^2)^2 + (N_{\dot{\phi}} + \alpha N_{\dot{\beta}})^2 \omega^2}$$

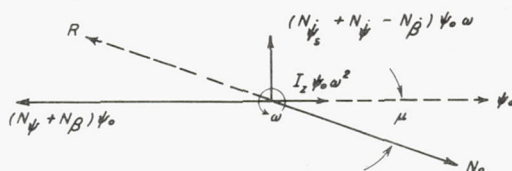
Sketch (d)

and the angle ξ is given by

$$\xi = \tan^{-1} \frac{(N_{\dot{\phi}} + \alpha N_{\dot{\beta}})\omega}{\alpha N_{\beta} + I_{xz} \omega^2}$$

The particular integral shows that ψ is also a harmonic function, and equation (12) states that the sum of the moments R , resulting from

the motion ψ must be equal and opposite to N_0 . The vector diagram is shown in sketch (e). The magnitude of the resulting yawing moment N_0 (which is equal to R) is



Sketch (e)

$$N_0 = \psi_0 \sqrt{(N_{\psi} + N_{\beta} - I_z \omega^2)^2 + (N_{\dot{\psi}_s} + N_{\dot{\psi}} - N_{\dot{\beta}})^2 \omega^2}$$

and the angle μ is given by

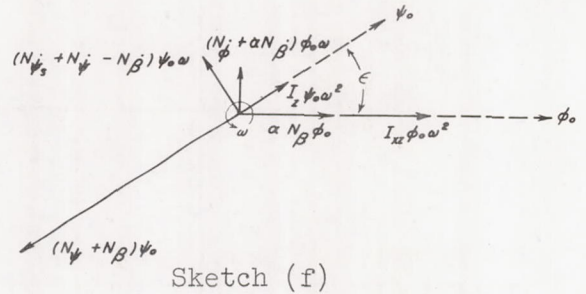
$$\mu = \tan^{-1} \frac{(N_{\dot{\psi}_s} + N_{\dot{\psi}} - N_{\dot{\beta}})\omega}{N_{\psi} + N_{\beta} - I_z \omega^2}$$

The amplitude ratio and phase angle given by equations (13) and (14) may then be written

$$\frac{\psi_0}{\phi_0} = \frac{N_0/\Phi_0}{N_0/\psi_0}$$

$$\epsilon = \xi + \mu$$

Equation (12) may now be represented by combining the vector diagrams shown in sketches (d) and (e). It can be seen that equations (15) and (16) represent the summations of the out-of-phase and in-phase components of the vector diagram of sketch (f).



The quantities in equations (15) and (16) measured during operation of the dynamic apparatus are Φ_0 , ψ_0 , ω , and ϵ . At any discrete frequency these are insufficient data to solve the equations; however, use of the apparatus as a free-oscillation system provides additional data from the complementary solution of equation (12):

$$\psi = \left\{ \exp \left[\frac{(N\dot{\psi}_s + N\dot{\psi} - N\dot{\beta})t}{2I_z} \right] \right\} \left\{ \psi_i \left[\cos \omega_a t - \frac{(N\dot{\psi}_s + N\dot{\psi} - N\dot{\beta})}{2I_z \omega_a} \sin \omega_a t \right] + \frac{\dot{\psi}_i}{\omega_a} \sin \omega_a t \right\} \quad (17)$$

where the angular frequency of oscillation is given by

$$\omega_a = \sqrt{\frac{N\dot{\psi} + N\dot{\beta}}{I_z} - \left(\frac{N\dot{\psi}_s + N\dot{\psi} - N\dot{\beta}}{2I_z} \right)^2} \quad (18)$$

For wind-off conditions, equations (17) and (18) may be written

$$\psi = \left[\exp \left(\frac{N\dot{\psi}_s}{2I_z} t \right) \right] \left[\psi_i \left(\cos \omega_n t - \frac{N\dot{\psi}_s}{2I_z \omega_n} \sin \omega_n t \right) + \frac{\dot{\psi}_i}{\omega_n} \sin \omega_n t \right] \quad (19)$$

where

$$\omega_n = \sqrt{\frac{N\dot{\psi}}{I_z} - \left(\frac{N\dot{\psi}_s}{2I_z} \right)^2} \quad (20)$$

The contribution of the system damping to the oscillation frequency is negligible, and equation (20) may be written

$$\omega_n = \sqrt{\frac{N_\psi}{I_z}}$$

The moment of inertia may then be evaluated:

$$I_z = \frac{N_\psi}{4\pi^2 f_n^2} \quad (21)$$

The system damping may be determined as

$$N_{\dot{\psi}_s}^* = \frac{2I_z}{\tau} \ln \left(\frac{\psi_T}{\psi_t} \right)_{\text{wind off}} \quad (22)$$

where ψ_T and ψ_t are ordinates of the envelope curve a time interval τ apart; similarly, the aerodynamic damping becomes

$$N_{\dot{\psi}} - N_{\dot{\beta}} = \frac{2I_z}{\tau} \ln \left(\frac{\psi_T}{\psi_t} \right)_{\text{wind on}} - N_{\dot{\psi}_s}^* \quad (23)$$

and the directional stability parameter N_β may be determined from equation (18):

$$N_\beta = 4\pi^2 I_z f_a^2 + \frac{(N_{\dot{\psi}_s}^* + N_{\dot{\psi}} - N_{\dot{\beta}})^2}{4I_z} - N_{\dot{\psi}} \quad (24)$$

Sufficient data are now available to solve equations (15) and (16) for wind-on conditions:

$$N_{\dot{\phi}} + \alpha N_{\dot{\beta}} = \frac{\psi_0}{\phi_0} \frac{(N_\psi + N_\beta - I_z \omega^2) \sin \epsilon - (N_{\dot{\psi}_s}^* + N_{\dot{\psi}} - N_{\dot{\beta}}) \omega \cos \epsilon}{\omega} \quad (25)$$

$$I_{xz} = \frac{\psi_0}{\phi_0} \frac{(N_\psi + N_\beta - I_z \omega^2) \cos \epsilon + (N_{\dot{\psi}_s}^* + N_{\dot{\psi}} - N_{\dot{\beta}}) \omega \sin \epsilon}{\omega^2} - \frac{\alpha N_\beta}{\omega^2} \quad (26)$$

It should be noted that the product of inertia I_{xz} may be obtained for wind-off conditions by elimination of the damping term in equations (15) and (16) to give

$$I_{xz} = \frac{\psi_0}{\phi_0} \frac{(N\dot{\psi} - I_z \omega^2)}{\omega^2 \cos \epsilon}$$

However, it was found that, for winged models at angle of attack, the slight elastic deformations of the model and support structure were sufficient to necessitate the use of equation (26).

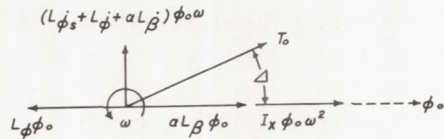
Roll equation.- The first of equations (11) may be rearranged and written as follows:

$$I_x \ddot{\phi} - (L\dot{\phi}_s + L\dot{\phi} + \alpha L\dot{\beta})\dot{\phi} + (L\phi - \alpha L\beta)\phi + I_{xz} \ddot{\psi} - (L\dot{\psi} - L\dot{\beta})\dot{\psi} + L\beta\psi = T \quad (27)$$

Before proceeding with the total equation (27), we will consider the case of single-degree-of-freedom roll motion, defined by equation (27) when ψ and its derivatives are identically zero. We proceed directly from the vector diagram given in sketch (g).

Summation of the out-of-phase and in-phase vector components gives

$$(L\dot{\phi}_s + L\dot{\phi} + \alpha L\dot{\beta})\phi_0 \omega + T_0 \sin \Delta = 0 \quad (28)$$



Sketch (g)

$$I_x \phi_0 \omega^2 - (L\phi - \alpha L\beta)\phi_0 + T_0 \cos \Delta = 0 \quad (29)$$

For wind-off conditions, equations (28) and (29) may be solved for

$$L\dot{\phi}_s = - \frac{T_0 \sin \Delta}{\phi_0 \omega} \quad (30)$$

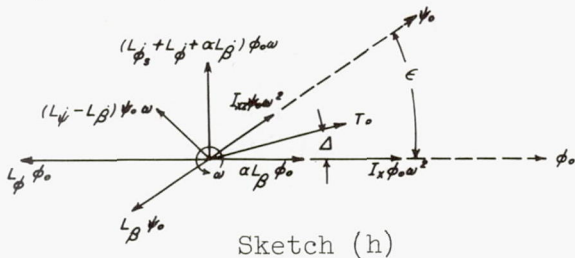
$$I_x = \frac{-T_0 \cos \Delta + L\phi\phi_0}{\phi_0 \omega^2} \quad (31)$$

For wind-on conditions,

$$L\dot{\phi} + \alpha L\dot{\beta} = - \frac{T_0 \sin \Delta}{\phi_0 \omega} - L\dot{\phi}_s \quad (32)$$

$$L\beta = \frac{1}{\alpha} \left(L\phi - \frac{T_0 \cos \Delta + I_x \phi_0 \omega^2}{\phi_0} \right) \quad (33)$$

Equation (33) becomes indeterminate at zero angle of attack; however, another expression for L_β may be obtained from the more general equation (27) which we now consider. The vector diagram representing equation (27) is shown in sketch (h). Summation of the out-of-phase and in-phase vector components gives



Sketch (h)

$$T_0 \sin \Delta + I_{xz} \psi_0 \omega^2 \sin \epsilon + (L_{\dot{\phi}_s} + L_{\dot{\phi}} + \alpha L_{\dot{\beta}}) \phi_0 \omega +$$

$$(L_{\dot{\psi}} - L_{\dot{\beta}}) \psi_0 \omega \cos \epsilon - L_{\beta} \psi_0 \sin \epsilon = 0 \quad (34)$$

$$T_0 \cos \Delta + (\alpha L_{\beta} - L_{\phi}) \phi_0 + I_x \phi_0 \omega^2 + I_{xz} \psi_0 \omega^2 \cos \epsilon -$$

$$(L_{\dot{\psi}} - L_{\dot{\beta}}) \psi_0 \omega \sin \epsilon - L_{\beta} \psi_0 \cos \epsilon = 0 \quad (35)$$

Multiplying equation (34) by $\sin \epsilon$, equation (35) by $\cos \epsilon$, and adding and solving for L_{β} gives

$$L_{\beta} = \frac{1}{\alpha \phi_0 \cos \epsilon - \psi_0} \left[(L_{\phi} - I_x \omega^2) \phi_0 \cos \epsilon - T_0 \cos(\Delta - \epsilon) - I_{xz} \psi_0 \omega^2 - (L_{\dot{\phi}_s} + L_{\dot{\phi}} + \alpha L_{\dot{\beta}}) \phi_0 \omega \sin \epsilon \right] \quad (36)$$

where the product of inertia I_{xz} is given by equation (26). Multiplying equation (34) by $\cos \epsilon$, equation (35) by $\sin \epsilon$, and subtracting and solving for $(L_{\dot{\psi}} - L_{\dot{\beta}})$ gives

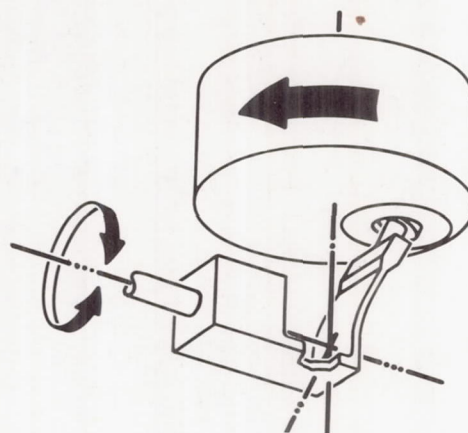
$$L_{\dot{\psi}} - L_{\dot{\beta}} = \frac{1}{\psi_0 \omega} \left[(\alpha L_{\beta} - L_{\phi} + I_x \omega^2) \phi_0 \sin \epsilon - (L_{\dot{\phi}_s} + L_{\dot{\phi}} + \alpha L_{\dot{\beta}}) \phi_0 \omega \cos \epsilon - T_0 \sin(\Delta - \epsilon) \right] \quad (37)$$

Description of Apparatus

A physical description of the drive apparatus and its various components is presented below. The next section deals with the functions of the instrumentation.

In discussing the drive apparatus, it is convenient to refer to the pictorial representation of the system presented in figure 2(b). The model is allowed two angular degrees of freedom (rolling and yawing), is subjected to constant-amplitude forced oscillations in roll, and is free to respond in yaw. It is rigidly restrained in pitch (at a constant angle of attack from 0° to 15°), and all externally applied pitching moments, lift, drag, and side forces are transmitted directly to the wind-tunnel structure. The apparatus is powered by a three-phase induction motor mounted vertically over the support-strut housing at the rear of the apparatus. Rotary motion of the motor shaft is converted to an approximate harmonic motion of the main drive shaft (torque tube) by means of the eccentric block and drive flexure indicated in the figure. An enlarged drawing of these components is shown in sketch (i) to aid in visualizing the principle involved.

Amplitude of the oscillatory rolling motion is determined by the amount of eccentricity in the eccentric block, and with the present system is 4° . The torque tube, which transmits the oscillatory motion to the model, is supported within the stationary support sting by the roll flexure pivots at the forward end and by a ball bearing at the rear. Rigidly attached to the front end of the torque tube are the yaw flexure pivots on which the model is mounted. The only contact between the model and the apparatus is through the mounting at the forward end of the yaw flexures; sufficient clearance exists between model body and support sting to allow the model to yaw approximately 2° about the flexure axis. The maximum operating frequency of the system is approximately 20 cycles per second.



Sketch (i)

To obtain accurate results with the system, it is necessary that rapid variations in oscillation frequency of the apparatus be eliminated. This purpose is served by the small flywheel shown mounted over the drive motor in figure 2(b).

To obtain accurate results with the system, it is necessary that rapid variations in oscillation frequency of the apparatus be eliminated. This purpose is served by the small flywheel shown mounted over the drive motor in figure 2(b).

The use of flexure pivots in the apparatus resulted primarily from the need for avoiding the often undesirable damping characteristics of ball bearings. The flexures used were designed in accordance with information presented in reference 9, and were found to be entirely satisfactory from the standpoint of defining a rigid axis of rotation.

Characteristics of flexure pivots.- The flexure pivots are designated as compensating type in reference 9 because, theoretically, the spring constant is essentially independent of load. The desirability of this feature in the present application is obvious, and the experimental verification is shown in figure 3 for the case of the yaw flexure pivots subjected to lift loads of 0, 100, and 200 pounds. The invariance of the roll-flexure-pivot spring constant was equally good.

The internal damping in the yaw flexure pivots was obtained by means of the well-known oscillation-decay method. It was found that the rate of decay was not logarithmic but, instead, was a function of both amplitude and frequency. However, equation (22) was applied to the data in order to obtain an equivalent viscous damping factor $N\dot{\psi}_S$. It was found that, as shown in figure 4, the data could be represented by an equation of the form

$$N\dot{\psi}_S = \frac{a + b\psi}{f} \quad (38)$$

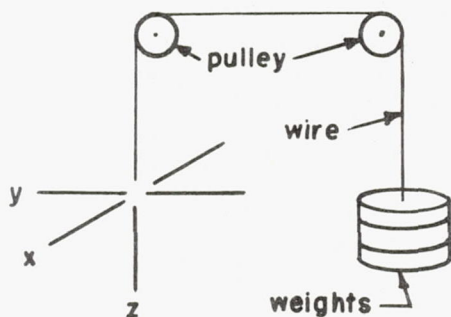
Justification for this type of expression can be seen by converting to the form given in reference 10 where the internal damping is presented in terms of a "damping capacity" Δw , the damping work per cycle per unit volume. This quantity was found to be independent of frequency and to vary as the third power of the stress amplitude. Consider the case of constant-amplitude oscillation, $\psi = \psi_0 \sin \omega t$. Then the damping capacity may be written (see, e.g., ref. 7) with the flexure-pivot cross-sectional area A and length h ,

$$\Delta w = \frac{N\dot{\psi}_S \psi_0^2 \omega^2}{Ah} \int_0^{2\pi} \frac{1}{\omega} \cos^2 \omega t \, dt = \frac{N\dot{\psi}_S \pi \psi_0^2 \omega}{Ah}$$

or,

$$\Delta w = \frac{(a + b\psi_0) 2\pi^2 \psi_0^2}{Ah} \quad (39)$$

Although Δw was found to vary in reference 10 primarily as the third power of the stress amplitude (which is directly proportional to the oscillation amplitude), examination of the results therein indicates that at the lower amplitudes the data may be approaching a second power variation as indicated by equation (39). Likewise, the damping capacity given by equation (39) is independent of frequency, and it is felt, therefore, that the use of the equivalent viscous damping factor represented by equation (38) is justified. The data presented in figure 4 also show



Sketch (j)

internal damping for the case of the yaw flexure pivots subjected to lift loads of 0, 100, and 200 pounds. The application of an external load which produces no additional damping is essentially impossible. However, it was found that the additional damping of a lift load simulated as shown in sketch (j) was negligible, and the data were obtained in this manner. Again it can be seen that there was essentially no effect of lift load.

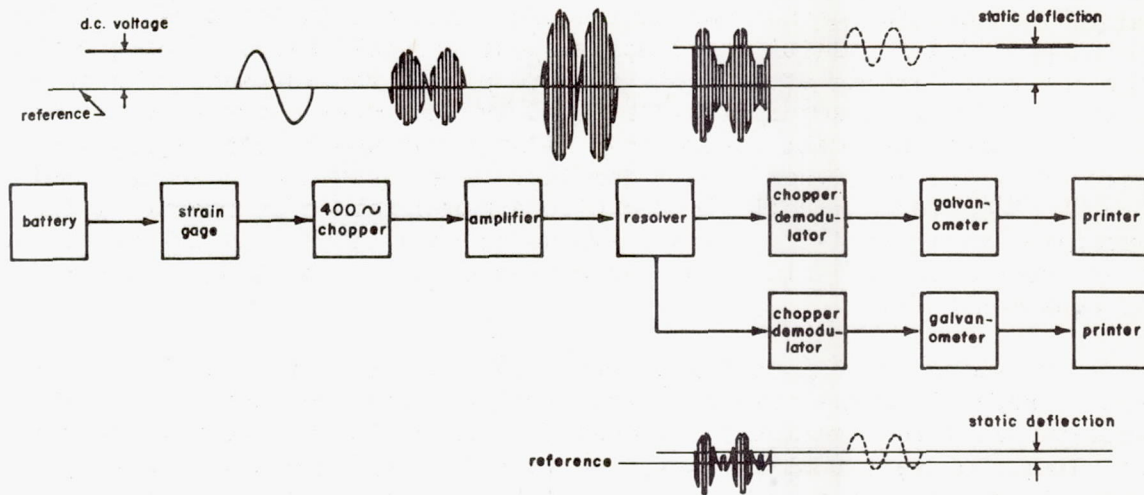
No successful method was devised for the application of a lift load which provided no additional damping about the roll axis. Consequently, the internal damping of the roll flexure pivots was assumed to be invariant with lift load, an assumption justified by the yaw-flexure results, and the fact that any small change that might occur would be a negligible percent of the aerodynamic roll damping. The equivalent viscous damping factor $L\dot{\phi}_S$ for the roll flexure pivots was obtained by operating the apparatus under wind-off, tunnel-evacuated conditions, and it was found that these results could also be represented by an equation of the form of equation (38).

The values of $L\dot{\phi}_S$ and $N\dot{\psi}_S$ were found to be approximately 20 percent and 12 percent, respectively, of the aerodynamic values obtained in the wind-tunnel investigation to be described later in the report. It should be noted, however, that the aerodynamic roll damping measured for the body-fin model used in the wind-tunnel test is much smaller than would be the case for a complete airplane model.

Instrumentation

Three quantities are measured by the system: angular roll and yaw positions of the model, and the roll-input torque applied to the model to maintain the forced oscillations in roll. These quantities are measured by means of resistance-type strain gages mounted on suitable beams, the locations of which are indicated in figure 2(b). The amplitudes and phase angles of the oscillating strain-gage signals are obtained by passing each of the signals through a sine-cosine resolver located at the drive motor and gear driven by the motor shaft (see fig. 2(b)). The two output signals of each resolver are then directly proportional to the in-phase and out-of-phase components of the respective strain-gage signals referenced to the resolver rotor position. By the vectorial summations of these quantities the required amplitudes of oscillation are obtained, as well as the phase relationships necessary to establish the roll-input-torque and yaw-position phase angles with respect to the model roll position. Oscillation frequency is measured by means of an electronic counter driven by a portion of the oscillating roll-position strain-gage signal.

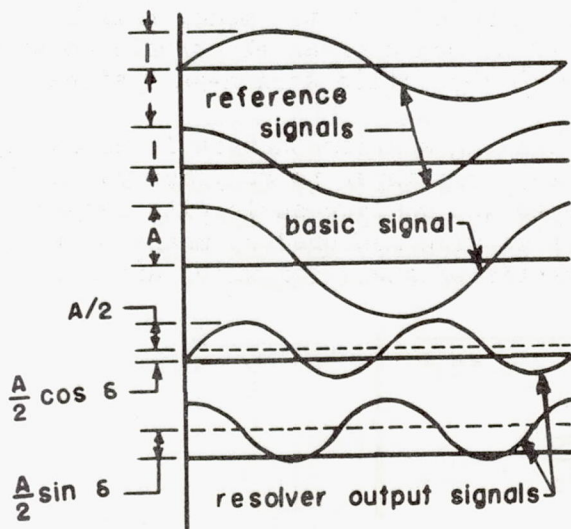
Circuits.- It was noted in the preceding section that it is necessary to know the amplitudes of the roll angle, roll-input torque, and yaw angle, and the phase angles of the roll-input torque and yaw angle with respect to the roll angle. The desired quantities were measured by means of three identical electronic circuits, the essential features of which are shown in sketch (k).



Sketch (k)

The principle of operation of the circuits is as follows: A direct voltage is impressed on the strain-gage bridge which is to provide a measurement of the desired quantity. The resulting output is an alternating voltage whose frequency is that at which the system is operating and whose magnitude is directly proportional to the amplitude of the desired quantity. This output is used to modulate a 400-cycle wave; the result is amplified and then passed through the resolver which reduces it to components in phase and out of phase with the position of the resolver rotor. These components are then demodulated and used to drive the galvanometers as shown in the sketch.

Resolvers.- The resolvers utilized in the apparatus were of the standard induction type, commercially available. Two coils are accurately positioned at 90° with respect to each other on the stator and, with a 1-to-1 transformer ratio, produce two harmonic signals also phased 90° when the rotor is turned at a constant angular speed.



Sketch (l)

The action of the resolver may be explained as follows: Assume the quantity to be measured, as represented by the oscillating strain-gage signal (hereafter referred to as the basic signal), has an amplitude of oscillation, A , and phase angle, δ , with respect to the resolver rotor. This signal is then defined as $A \sin(\omega t + \delta)$. The resolver may be considered to provide two reference signals of unit amplitude, $\sin \omega t$, $\cos \omega t$ as shown in sketch (l). Transmission

of the basic signal through the resolver effectively results in multiplication of the basic signal with the two reference signals:

$$\begin{aligned} V_i &= A \sin(\omega t + \delta) \sin \omega t \\ &= \frac{A}{2} \cos \delta - \frac{A}{2} \cos(2\omega t + \delta) \end{aligned} \quad (40)$$

$$\begin{aligned} V_o &= A \sin(\omega t + \delta) \cos \omega t \\ &= \frac{A}{2} \sin \delta + \frac{A}{2} \sin(2\omega t + \delta) \end{aligned} \quad (41)$$

Thus the amplitudes of the resolver output signals are one half that of the basic signal, the frequencies are twice the frequency of operation of the system, and each of the resultant signals has been displaced, the first by an amount equal to one half the product of the basic signal and the cosine of the phase angle, the second by one half the product of the basic signal and the sine of the phase angle.

Equations (40) and (41), which represent the components of the basic strain-gage signal in phase and out of phase with the resolver rotor position, also represent the time-varying voltages used to drive the galvanometers as shown in sketch (k).

Galvanometers.— A galvanometer element is essentially a single-degree-of-freedom system, and its amplitude and phase-angle responses to a harmonically varying forcing function are well known. If the frequency given in equations (40) and (41) is much greater than the undamped natural frequency of the galvanometer element, the response of the element to that portion of the signal will be essentially zero. The first term on the right-hand side of each of equations (40) and (41) represents a voltage which is independent of time, however, and the galvanometer is capable of responding with a deflection G which is directly proportional to the static signal. The results, as shown in sketch (k), are static indications of the in-phase and out-of-phase components of the harmonically varying quantity.

Application of the proper calibration constants C_o and C_i now permits the computation of the amplitude and phase angle of the desired quantity, the amplitude being equal to the square root of the sum of the squares of the in-phase and out-of-phase components, and the tangent of the phase angle being given by the ratio of the out-of-phase to in-phase components:

$$\left. \begin{aligned} A &= 2\sqrt{C_i^2 G_i^2 + C_o^2 G_o^2} \\ \delta &= \tan^{-1} \frac{C_o G_o}{C_i G_i} \end{aligned} \right\} \quad (42)$$

The phase angle thus obtained are those between the resolver rotors and each of the measured quantities; roll position, yaw position, and roll-input torque. It will be recalled, however, that the desired phase angles are those between the yaw position and roll positions, and between the roll-input torque and roll position. It is clear that these quantities are immediately obtainable from the above information if the relative phase angles of the three resolvers with respect to each other are known. Since it is convenient to the operation of the system to maintain these relative phase differences at small values, the resolvers are first aligned with each other as accurately as possible. A calibration is then made from which the remaining phase angles are obtained.

Effects of harmonics.- When the principle of operation of the resolver circuits was illustrated, it was assumed that the basic signal was a pure harmonic function. In general, the quantities to be measured are not pure harmonic functions, but may be distorted due to extraneous disturbances from support vibration and other sources, one of which was the slightly impure harmonic motion of the model produced by the eccentric block and drive flexure in converting the rotary motion of the motor into an oscillatory motion of the torque tube. In addition, the voltage output of the strain-gage bridge may have a mean value other than zero due to initial unbalance of the bridge. The voltage output may then be represented by the Fourier series

$$A_0 + \sum_{n=1}^{\infty} (a_n \cos n\omega t + b_n \sin n\omega t)$$

or, in a more convenient form,

$$A_0 + \sum_{n=1}^{\infty} A_n \sin(n\omega t + \delta_n) \quad (43)$$

where

$$A_n = \sqrt{a_n^2 + b_n^2}$$

$$\delta_n = \tan^{-1} \frac{b_n}{a_n}$$

In a similar manner, the resolver reference signals may not be pure harmonic functions; if, in addition, the two reference signals are not phased exactly 90° with respect to each other, but have some other phase angle γ , the Fourier series representing the two signals may be written

$$\sum_{m=1}^{\infty} B_m \sin m\omega t \quad (44)$$

$$\sum_{m=1}^{\infty} B_m \sin(m\omega t + \gamma) \quad (45)$$

Then the in-phase and out-of-phase voltages used to drive the galvanometers will be given by the products of equations (43) and (44), and (43) and (45), respectively:

$$\begin{aligned} V_i &= A_0 \sum_{m=1}^{\infty} B_m \sin m\omega t + \sum_{n=1}^{\infty} \sum_{m=1}^{\infty} A_n B_m \sin(n\omega t + \delta_n) \sin m\omega t \\ &= A_0 \sum_{m=1}^{\infty} B_m \sin m\omega t + \sum_{n=1}^{\infty} \sum_{m=1}^{\infty} \frac{A_n B_m}{2} \left\{ \cos \left[(n - m)\omega t + \delta_n \right] - \right. \\ &\quad \left. \cos \left[(n + m)\omega t + \delta_n \right] \right\} \end{aligned} \quad (46)$$

$$\begin{aligned} V_o &= A_0 \sum_{m=1}^{\infty} B_m \sin(m\omega t + \gamma) + \sum_{n=1}^{\infty} \sum_{m=1}^{\infty} A_n B_m \sin(n\omega t + \delta_n) \sin(m\omega t + \gamma) \\ &= A_0 \sum_{m=1}^{\infty} B_m \sin(m\omega t + \gamma) + \sum_{n=1}^{\infty} \sum_{m=1}^{\infty} \frac{A_n B_m}{2} \left\{ \cos \left[(n - m)\omega t + \delta_n - \gamma \right] - \right. \\ &\quad \left. \cos \left[(n + m)\omega t + \delta_n + \gamma \right] \right\} \end{aligned} \quad (47)$$

Examination of equations (46) and (47) reveals that time-independent voltages occur only when $n = m$, that is, for products of equal harmonics. Then the effective voltages, those to which the galvanometers will respond, may be written

$$V_i = \sum_{n=1}^{\infty} \frac{\cos \delta_n}{2} A_n B_n \quad (48)$$

$$V_o = \sum_{n=1}^{\infty} \frac{\cos(\delta_n - \gamma)}{2} A_n B_n \quad (49)$$

These equations show that the in-phase and out-of-phase components of each measured quantity may be in error by an amount equal to the sum of the products of equal harmonics contained in the quantity to be measured and in the resolver signals. If either of the signals has no harmonic content, but consists only of the fundamental ($n = 1$), no error is caused irrespective of the distortion present in the other. Under normal wind-tunnel operating conditions it would be expected that, due to previously mentioned disturbances, some distortion would be present in the basic signals, and it is necessary that the resolver signals be free of all comparable harmonics in order to eliminate this possible source of error. For this reason the resolvers were driven by 90-tooth gears. A remaining possible source of low-frequency harmonic content in the resolver signals was slip ring "noise"; a visual examination of the resolver reference signals by means of an oscilloscope revealed no distortion, however. One other possible error due to the resolvers is indicated in equation (49): the phasing of the resolver reference signals with respect to each other by some angle γ other than 90° . For the resolvers used in the present investigation the angle γ was accurate to $90^\circ \pm 1/2^\circ$, and the error from this source was, therefore, negligible. Now, since the fundamental amplitude, B_1 , of the resolver reference signals is unity, equations (48) and (49) simplify to

$$V_i = \frac{A_1}{2} \cos \delta_1$$

$$V_o = \frac{A_1}{2} \sin \delta_1$$

The galvanometer deflections G_i and G_o are directly related to the in-phase and out-of-phase voltages by the appropriate calibration constants C_i and C_o . The amplitude and phase angle are given by

$$\left. \begin{aligned} A_1 &= 2 \sqrt{C_o^2 G_o^2 + C_i^2 G_i^2} \\ \delta_1 &= \tan^{-1} \frac{C_o G_o}{C_i G_i} \end{aligned} \right\} \quad (50)$$

Equations (50) are identical with equations (42) which were developed for the case of no distortion in the quantities to be measured. It can be seen that the system, in effect, filters out the unwanted harmonics and provides a measure only of the desired response.

Frequency characteristics.- Mention was made of the alinement and calibration necessary to determine the final phase relationships of the resolvers. The method of alining the resolvers is as follows: While the oscillation frequency is maintained at some constant value, each of the three circuits is, in turn, connected to the output of the roll-position gage. In each case the appropriate resolver housing is then rotated until the out-of-phase component indicated on the galvanometer is approximately zero and is locked in this position. In conjunction with these operations a check was also obtained on the frequency characteristics of the measuring circuits. It should be recalled that the phase angles necessary for data reduction are measured with respect to the roll position. Then it is clear that the absolute value and frequency dependence of the phase angles indicated by the resolver circuits is immaterial if these characteristics are identical for each circuit. The procedure was as follows: After alining the resolvers, each of the circuits was, in turn, connected to the output of the roll-position gage, and the amplitude and phase angle were computed for discrete frequencies covering the available range of operation. It was found that the phase shift varied slightly for the three circuits, the phase angle differences varying in a manner linear with frequency. The phase shift difference was then used as a calibration for correcting the phase angles obtained during testing.

Operation of the System

The operational procedures followed in conducting wind-tunnel investigations with the testing apparatus are described briefly below. It should be noted that the procedures are essentially identical when the apparatus is used for calibration tests such as are described in a later section.

(1) With the model rigidly restrained in yaw, measurements of roll position ϕ , roll-input torque T , and the roll-input-torque phase angle Δ are obtained for single-degree-of-freedom roll oscillations, at discrete frequencies throughout the available range, by means of the resolver circuits previously described. Data thus obtained, for both wind-off tunnel-evacuated, and wind-on conditions, and the calibrated roll-flexure spring constant, L_ϕ , provide $L_{\dot{\phi}_S}$ and I_x from equations (30) and (31), $L_{\dot{\phi}} + \alpha L_\beta$ from equation (32), and, for angle of attack other than zero, L_β from equation (33).

(2) With the model free to yaw, the model is driven in roll at the yaw natural frequency. When the model has attained sufficient yawing amplitude, the drive motor providing the oscillatory rolling motion is stopped abruptly, resulting in a single-degree-of-freedom free-yaw oscillation. A time history of the decaying yawing motion is obtained by means of a recording oscillograph. Again these data are obtained for both wind-off tunnel-evacuated and wind-on conditions, and with them and the calibrated yaw-flexure spring constant, N_ψ , equations (21) through (24) yield I_z , $N_{\dot{\psi}_S}$, $N_{\dot{\psi}} - N_\beta$, and N_β , respectively.

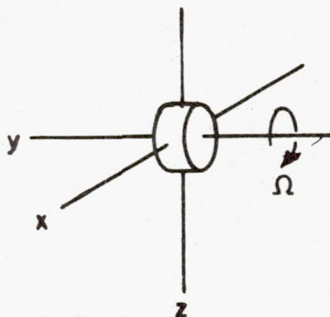
(3) With the model free to yaw, the apparatus is operated as a two-degree-of-freedom system at discrete frequencies throughout the operating range. At each frequency measurements of the roll position ϕ , yaw position ψ , roll-input torque T , and the phase angles ϵ and Δ are obtained by means of the resolver circuits. Use of these data in conjunction with those obtained from (1) and (2) above provides $N_{\dot{\phi}} + \alpha N_{\dot{\beta}}$ and I_{xz} from equations (25) and (26), $L_{\dot{\beta}}$ and $L_{\dot{\psi}} - L_{\dot{\beta}}$ from equations (36) and (37).

EVALUATION OF SYSTEM

It should be noted that the aerodynamic moments produced by angular velocities are, in general, much smaller than the moments produced by angular displacements, and the disturbances inevitably present in any wind tunnel may be of the order of magnitude of the quantities to be measured. An analysis of the manner in which the effects of these disturbances are eliminated in the present system has been discussed in the section on instrumentation. The results of such analyses are not sufficient information to determine completely the over-all accuracy; however, a reliable indication of the accuracy can be obtained where it is possible to simulate the quantities to be measured with known inputs to the system. The results of tests of this type will be discussed. A further check of the system accuracy when operating under wind-tunnel conditions was obtained through the testing of a simple configuration for which, it was felt, certain of the aerodynamic derivatives could be calculated fairly accurately. The results of these tests are discussed at the end of this section.

Evaluation of the System With Simulated Aerodynamic Derivatives

Cross derivatives $N_{\dot{\phi}}$ and $L_{\dot{\psi}}$.— Tests with the simulated aerodynamic derivatives were made in order to assess the accuracy of the system and the validity of the assumptions made in the linearization of the equations of motion. The aerodynamic cross derivatives $N_{\dot{\phi}}$ and $L_{\dot{\psi}}$ were simulated by means of a variable-speed gyroscopic motor as indicated in sketch (m).



Sketch (m)

The torque due to precession of a gyroscope is well known (see, e.g., ref. 8), and it is this property which was utilized in the present application. The gyroscope was mounted in place of the model, and, with the rotor oriented as shown, the simulated cross derivatives provided by the gyro are given by

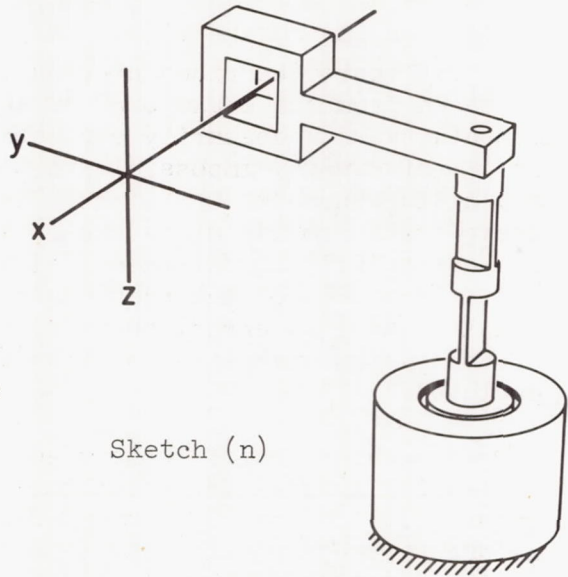
$$L_{\dot{\psi}} = -N_{\dot{\phi}} = I \Omega$$

where

- I rotor moment of inertia
- Ω angular velocity of rotor

The results of the gyroscope calibration are shown in figure 5 where the range of values given is expected to cover all possible wind-tunnel results. It can be seen from figure 5 that the accuracy with which $N\dot{\phi}$ is determined is entirely satisfactory. It was found that the values of $L\dot{\psi}$ obtained from equation (37) were unreliable, however, and these results are not presented. This was also found to be true for the calculation of $L\beta$ from equation (36) and a re-examination of the method of determining these derivatives will be necessary.

Damping-in-roll derivative $L\dot{\phi}$. - The results of tests in which the aerodynamic roll damping $L\dot{\phi}$ was simulated are shown in figure 6. This derivative was simulated in the manner indicated in sketch (n). A moment proportional to the angular velocity $\dot{\phi}$ was produced about the x axis by means of a magnetic damper acting through a flexure-pivot universal joint on an arm connected rigidly to the roll torque tube. The damping moment was generated by operating the system with a direct-current field excitation and a short-circuited armature. If the current generated in the armature and the armature resistance are designated as I and R, respectively, the simulated aerodynamic derivative may be expressed, for small angular displacement ϕ , as



$$L\dot{\phi} = \frac{2\pi c I^2 R}{\phi_0^2 \omega^2}$$

where c is the conversion from joules to inch-pounds. With the damper inoperative, an equivalent damping factor was obtained for the internal friction in the roll flexure pivots, universal joint, and flexible mounting of the damper armature. This quantity was subtracted from the damper-on data to give the results shown in figure 6. These results show the accuracy with which the system measures the simulated aerodynamic derivative $L\dot{\phi}$ in the absence of tunnel disturbances.

Damping in yaw and directional stability derivatives $C_{nr} - C_{n\beta}$ and $C_{n\beta}$. - No satisfactory method was found for introducing simulated values of aerodynamic yaw damping and directional stability into the system during the previously described tests, and it is, therefore, necessary

to analyze the results of the wind-tunnel tests, described in the following sections, to determine the accuracy with which these derivatives were obtained. The procedures for obtaining and reducing free-oscillation data are well known, as are the factors affecting the accuracy of these data. The uncertainties in each of the measured quantities present in the equation defining $C_{n_r} - C_{n_{\dot{\beta}}}$ and $C_{n_{\beta}}$ have been calculated. The square root of the sum of the squares of these uncertainties indicated over-all uncertainties of the order of ± 0.055 and ± 0.057 for single values of $C_{n_r} - C_{n_{\dot{\beta}}}$ and $C_{n_{\beta}}$, respectively. Not accounted for in these values, however, are possible effects of random air-stream disturbances and support vibrations which would appear as scatter in the data. The standard deviation of a number of observations at a given Mach number was, therefore, calculated; this was found to be of the order of ± 0.127 for $C_{n_r} - C_{n_{\dot{\beta}}}$ and ± 0.028 for $C_{n_{\beta}}$.

Evaluation of the System in the Wind Tunnel

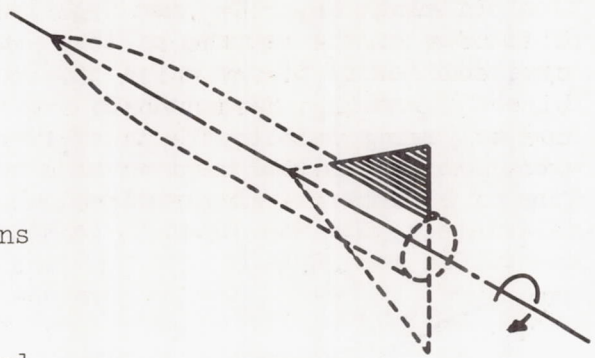
The tests described previously, in which the system accuracy was assessed from the standpoint of ability to measure simulated aerodynamic moments, were necessarily conducted under somewhat idealized conditions. It is, of course, impossible to simulate all of the loading conditions and disturbances to which the model is subjected in the wind tunnel, and these tests provide a measure of the accuracy of the system when there are essentially no extraneous disturbances present. It has been shown in the analysis of the previous section that these disturbances, theoretically, cause no error; however, it is desirable to check the capabilities of the system operating in the wind-tunnel environment for which it was designed.

An evaluation of the system in the wind tunnel necessarily depends on testing a model for which the aerodynamic derivatives may be calculated accurately. It is, of course, realized that an exact check on the system accuracy is not possible by this means since present theoretical knowledge is insufficient to permit exact calculations of the lateral dynamic stability derivatives of fin-body combinations; a serious decrease of the system accuracy due to tunnel disturbances should, however, be evident.

For the tests described below, a simple model was constructed for which, it was felt, the rolling-velocity derivatives C_{l_p} and C_{n_p} could be estimated with a fair degree of accuracy. The model, which consisted of a vertical triangular fin mounted on a cylindrical body with an ogival nose (see fig. 7), was tested with the dynamic system in the Ames 6- by 6-foot supersonic wind tunnel over a range of subsonic and supersonic Mach numbers at zero angle of attack.

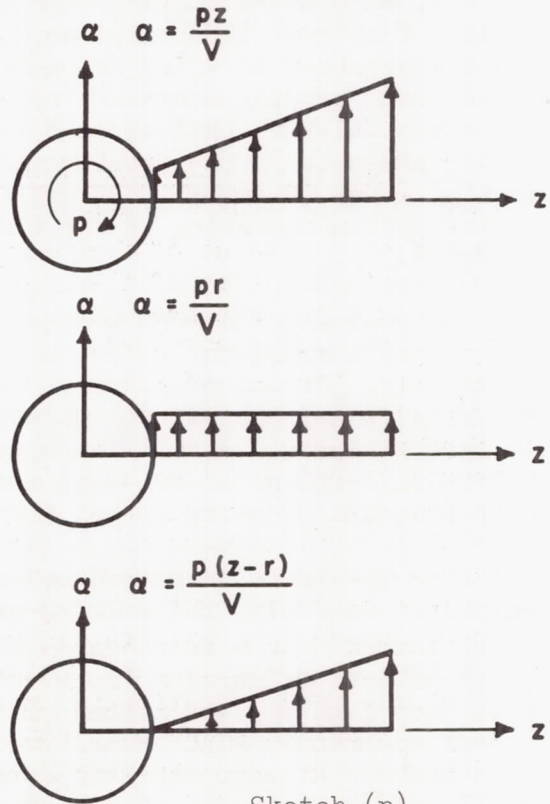
Estimation of stability derivatives.- Estimation of the stability derivatives was based on existing theoretical methods adapted to the particular model used in the wind-tunnel tests. The following is a brief description of the methods by which the derivatives were estimated.

In determining the roll-velocity derivatives, C_{l_p} and C_{n_p} , it was assumed that the fin acts as a portion of a rolling triangular wing as indicated in sketch (o). The solution for the resulting pressure distribution is well known (see, e.g., ref. 11) and was used directly to calculate the damping-in-roll derivative C_{l_p} and the contribution of the fin to the cross derivative C_{n_p} . Pressures induced on the body by the loading on the fin of course provide no rolling moment, but contribute directly to the yawing moment, and, therefore, must be considered in estimating C_{n_p} for the fin-body combination. Methods are available for computing the interference load distribution for fin-body combinations at supersonic speeds (refs. 12, 13, and 14) but these are, in general, very laborious and for this reason the method described below was applied in the present case.



Sketch (o)

It was assumed that the pressures induced on the body could be calculated as though the body were a flat plate at zero angle of attack adjacent to the fin. Reference 15 gives the solution for a case similar to this, namely the pressure distribution induced on a flat plate at zero angle of attack adjacent to a triangular sector at a constant angle of attack. The angle-of-attack distribution on the fin may be represented as the sum of a constant angle of attack ($\alpha = \frac{Pr}{V}$) and one which increases linearly in the spanwise direction ($\alpha = \frac{pz}{V}$) as shown in sketch (p).

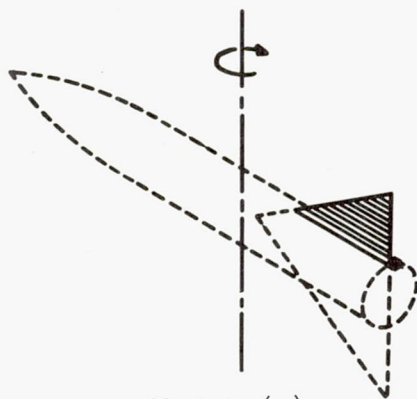


Sketch (p)

The pressure induced on the body by the constant angle-of-attack distribution is given directly by the solution in reference 15. The induced pressure resulting from the effective twist due to rolling velocity may be found by integrating across the span of the wing. This integration corresponds to the superposition of an infinite number of the lifting sectors along the span, each sector having an infinitesimal angle of attack. The yawing moment due to the induced pressures on the body was added to that

due to the loading on the fin to obtain the total yawing moment due to roll velocity. Because of the approximations necessary in the above estimate, the yawing moment due to rolling velocity was also calculated using the slender-body theory of reference 16 in order to provide a check of the order of magnitude.

In estimating the yawing derivatives it was assumed (a) that, in lieu of a more exact theory, the yawing moment of the body is that given by slender-body theory which, of course, is known to be incorrect at the higher supersonic Mach numbers and (b) that the yawing moment of the fin due to yawing velocity is that given by the moment, about the appropriate axis, of the loading on a portion of a pitching wing. Sketch (q) shows the portion of the wing referred to as a cross-hatched area and the



Sketch (q)

pitching axis as the axis of yaw. The loading was calculated according to reference 17 for the arrangement as shown to determine the yawing moment due to yawing velocity. A similar method was used for estimating the yawing moment due to sideslip angle. The slender-body-theory results were obtained from reference 18. The above methods, of course, applied only to the derivatives for supersonic Mach numbers. No methods were available of sufficient accuracy to permit the estimation of the derivatives at subsonic Mach numbers.

Comparison of estimated stability derivatives with measured values.-

During the wind-tunnel tests the rolling derivatives C_{l_p} and C_{n_p} were obtained over a range of frequencies from 7 to 20 cycles per second. No significant variation of these quantities with frequency was found, and the values which are presented in figures 8 and 9 are the arithmetic mean of the values obtained. The values of $C_{n_r} - C_{n\dot{\beta}}$ and $C_{n\dot{\beta}}$ are those which were obtained at a single frequency through free-oscillation tests. A comparison of the estimated and measured rolling derivatives is given in figures 8 and 9 for the supersonic Mach numbers investigated. The measured values are also shown for the subsonic Mach numbers. The agreement between the experimental and estimated values indicates that there were no serious effects of wind-tunnel disturbances on the system accuracy. Figure 10 shows the measured and estimated damping in yaw. Here the agreement is poor, particularly at the highest Mach number. The same is true of the directional stability parameter $C_{n\dot{\beta}}$, shown in figure 11, where the agreement is satisfactory except at the highest Mach number. The methods used in estimating the theoretical values of the derivatives may not be reliable and have not been adequately checked experimentally. A large part of the discrepancy between theory and experiment is believed to be due to deficiencies in the theory.

CONCLUSIONS

A study of a system designed to measure the static and dynamic lateral stability derivatives has lead to the following conclusions:

1. Tests in which aerodynamic derivatives were simulated have shown that the apparatus correctly measures known inputs of the order of magnitude anticipated for airplane models.

2. The investigation has shown that the aerodynamic derivatives associated with the primary mode of operation of the system, that is the rolling derivatives, and the directional-stability and damping-in-yaw parameters may be obtained with satisfactory accuracy. The data-reduction equations from which the rolling moment due to yawing velocity and due to sideslip angle were determined yielded results which were unreliable and prevented evaluation of C_{l_r} - $C_{l_{\dot{\beta}}}$ and $C_{l_{\beta}}$.

3. Tests of the apparatus utilizing a simple model showed that the wind-tunnel environment apparently had no deleterious effects on the system accuracy.

Ames Aeronautical Laboratory
National Advisory Committee for Aeronautics
Moffett Field, Calif., Sept. 24, 1954.

REFERENCES

1. Bradfield, F. B.: Lateral Control of Bristol Fighter at Low Speeds. Measurement of Rolling and Yawing Moments of Model Wings Due to Rolling. R. & M. No. 787, British A.R.C., 1921.
2. Bryant, L. W., and Halliday, A. S.: Measurement of Lateral Derivatives on the Whirling Arm. R. & M. No. 1249, British A.R.C., 1929.
3. Relf, E. F., Lavender, T., and Ower, E.: The Determination of Rotary Derivatives, with an Appendix on Approximate Formulae for Rotary Derivatives, by H. Glauert. R. & M. No. 809, British A.R.C., 1921.
4. Beam, Benjamin H.: A Wind-Tunnel Test Technique for Measuring the Dynamic Rotary Stability Derivatives Including the Cross Derivatives at High Mach Numbers. NACA TN 3347, 1954.
5. Bird, John D., Jaquet, Byron M., and Cowan, John W.: Effect of Fuselage and Tail Surfaces on Low-Speed Yawing Characteristics of a Swept-Wing Model as Determined in the Curved-Flow Test Section of the Langley Stability Tunnel. NACA TN 2483, 1951.

6. MacLachlan, Robert, and Letko, William: Correlation of Two Experimental Methods of Determining the Rolling Characteristics of Unswept Wings. NACA TN 1309, 1947.
7. Rauscher, Manfred: Introduction to Aeronautical Dynamics. John Wiley and Sons, Inc., N. Y., 1953.
8. Den Hartog, Jacob Pieter: Mechanical Vibrations. Third ed., McGraw-Hill Book Co., Inc., N. Y., 1947.
9. Eastman, Fred Scoville: Flexure Pivots to Replace Knife Edges and Ball Bearings. An Adaptation of Beam-Column Analysis. Univ. of Washington, Engineering Experiment Station Series. Bull. 86, Nov. 1935.
10. Robertson, J. M., and Yorgiadis, A. J.: Internal Friction in Engineering Materials. Jour. Appl. Mech., vol. 13, no. 3, Sept. 1946, pp. A173-A182.
11. Brown, Clinton E., and Adams, Mac C.: Damping in Pitch and Roll of Triangular Wings at Supersonic Speeds. NACA Rep. 892, 1948. (Supersedes NACA TN 1566.)
12. Nielsen, Jack N., and Pitts, William C.: Wing-Body Interference at Supersonic Speeds With an Application to Combinations With Rectangular Wings. NACA TN 2677, 1952.
13. Ferrari, Carlo: Interference Between Wing and Body at Supersonic Speeds - Theory and Numerical Application. Jour. Aero. Sci., vol. 15, no. 6, June 1948, pp. 317-336.
14. Morikawa, George K.: The Wing-Body Problem for Linearized Supersonic Flow. C.I.T., Pasadena, Guggenheim Aeronautical Lab., Doctoral Thesis, 1949.
15. Lagerstrom, P. A.: Linearized Supersonic Theory of Conical Wings. NACA TN 1685, 1950. Issued also as: C.I.T., Pasadena, (Guggenheim Aeronautical Lab.), Jet Propulsion Lab. PR 4-36, Dec. 1947.
16. Sacks, Alvin H.: Aerodynamic Forces, Moments, and Stability Derivatives for Slender Bodies of General Cross Section. NACA TN 3283, 1954.
17. Bobbitt, Percy J.: Theoretical Calculations of the Lateral Stability Derivatives for Triangular Vertical Tails With Subsonic Leading Edges Traveling at Supersonic Speeds. NACA TN 3240, 1954.
18. Miles, J. W.: The Application of Unsteady Flow Theory to the Calculation of Dynamic Stability Derivatives. North Amer. Aviation, Inc., Los Angeles. Aerophysics Lab. AL-957, Sept. 1950.

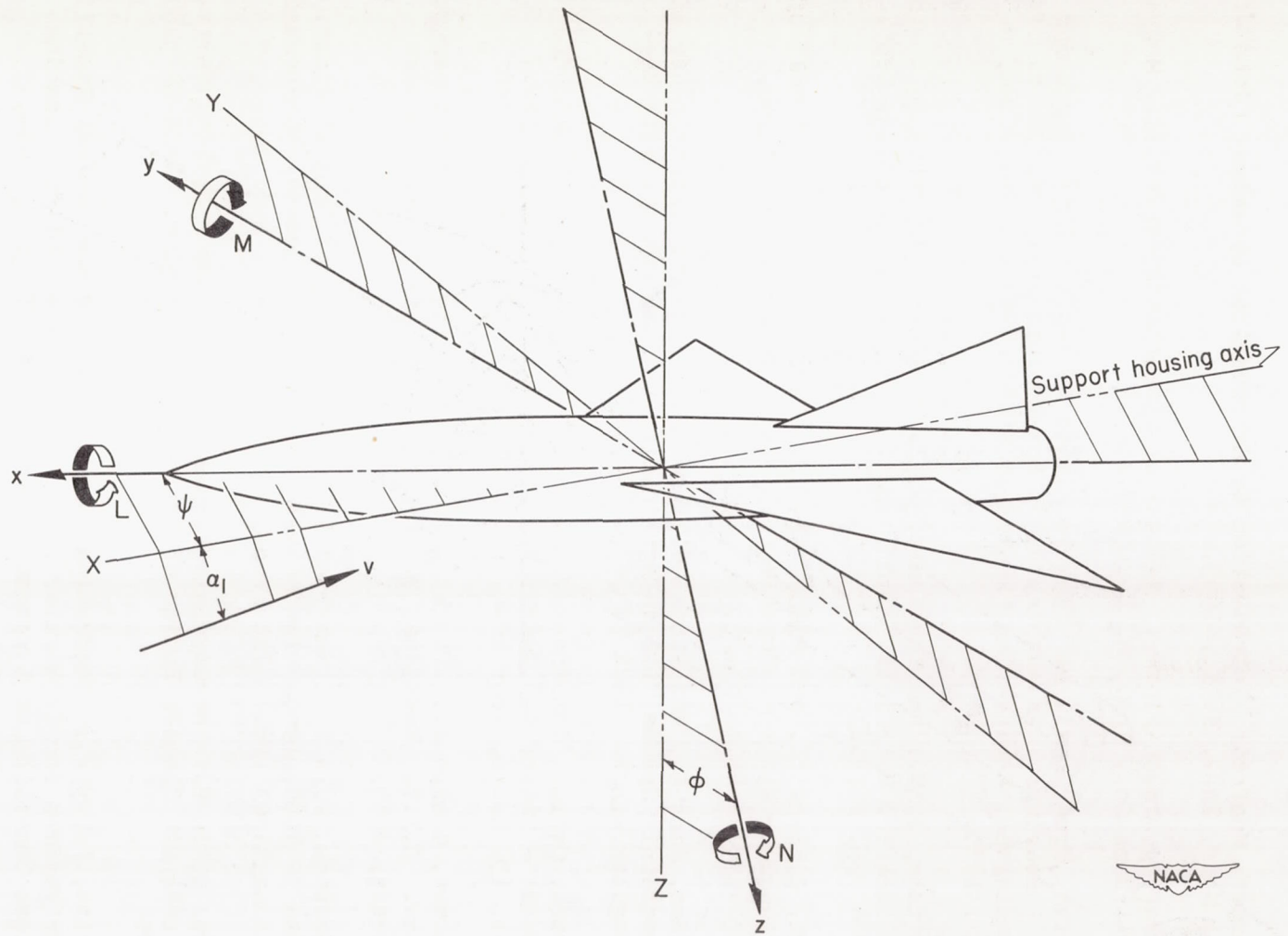
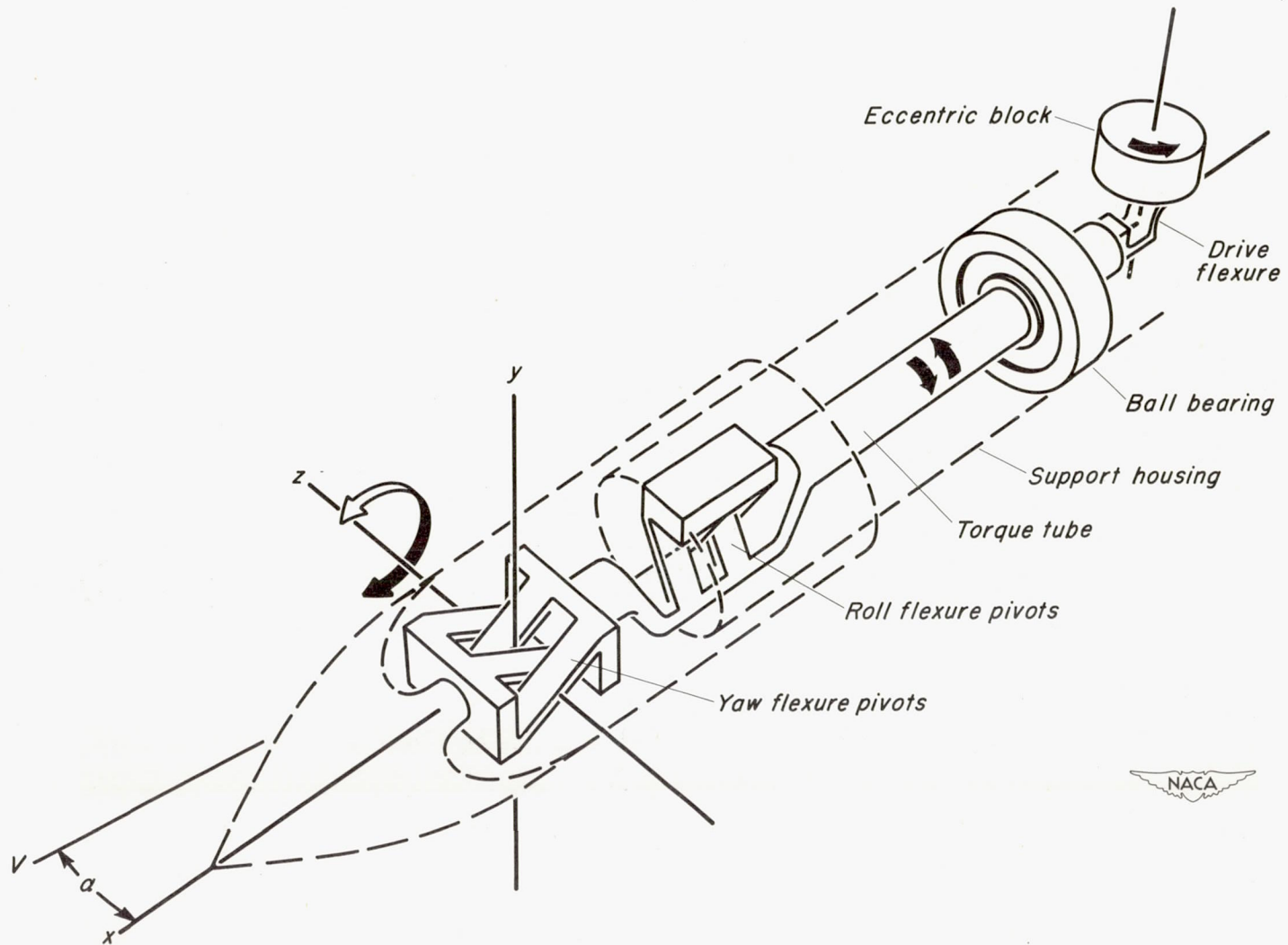
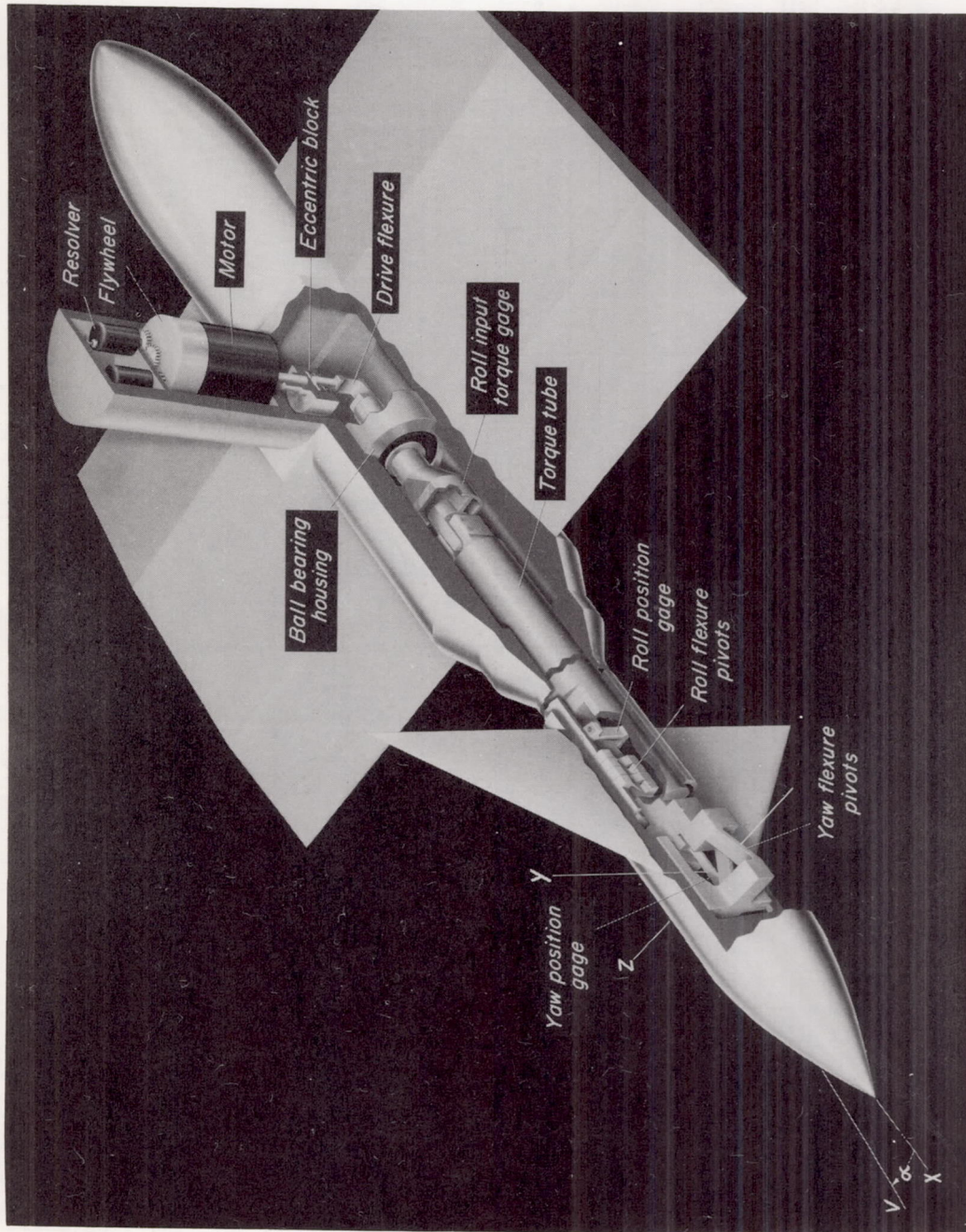


Figure 1.- Illustration of coordinate system. Displacements and moments are shown in the positive sense.



(a) Schematic drawing.

Figure 2.- Illustration of dynamic testing apparatus.



A-18673.1

(b) Pictorial drawing.

Figure 2.- Concluded.

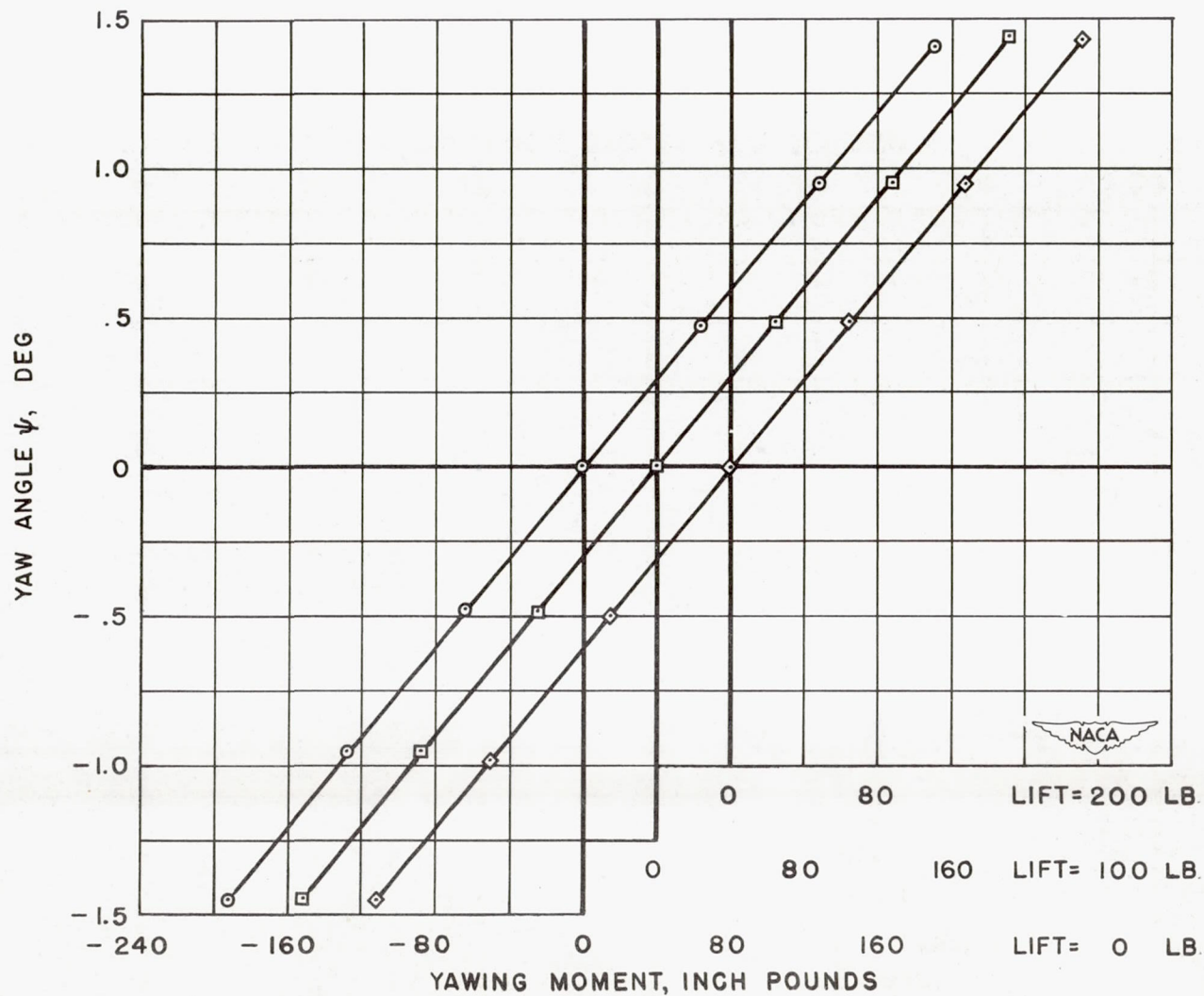


Figure 3.- Effect of simulated lift load on yaw flexure pivot spring constant.

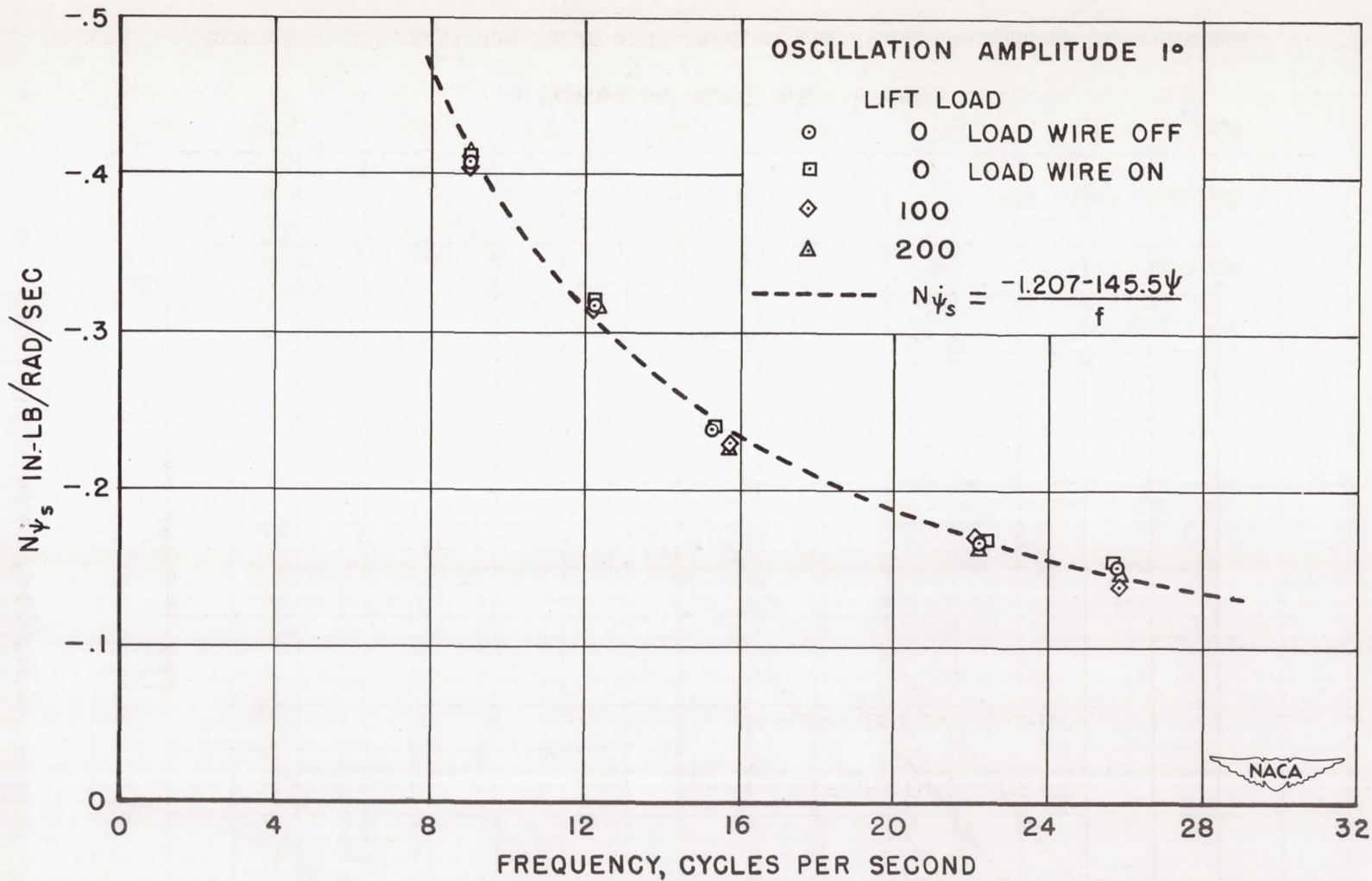


Figure 4.- Effect of simulated lift load on the internal damping of the yaw flexure pivots.

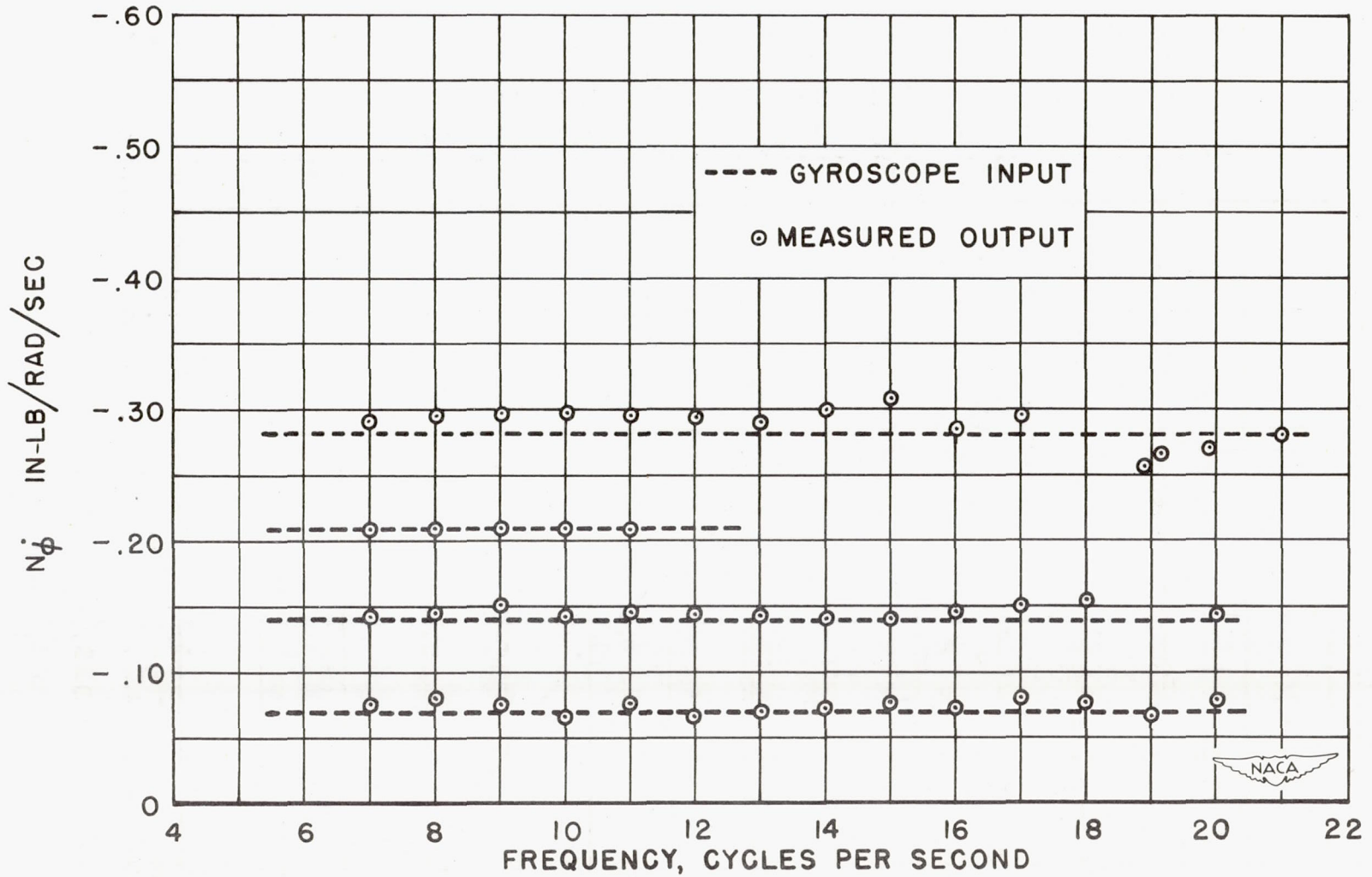


Figure 5.- Comparison of gyroscope input and measured output of the simulated aerodynamic cross derivative $N_{\dot{\phi}}$.

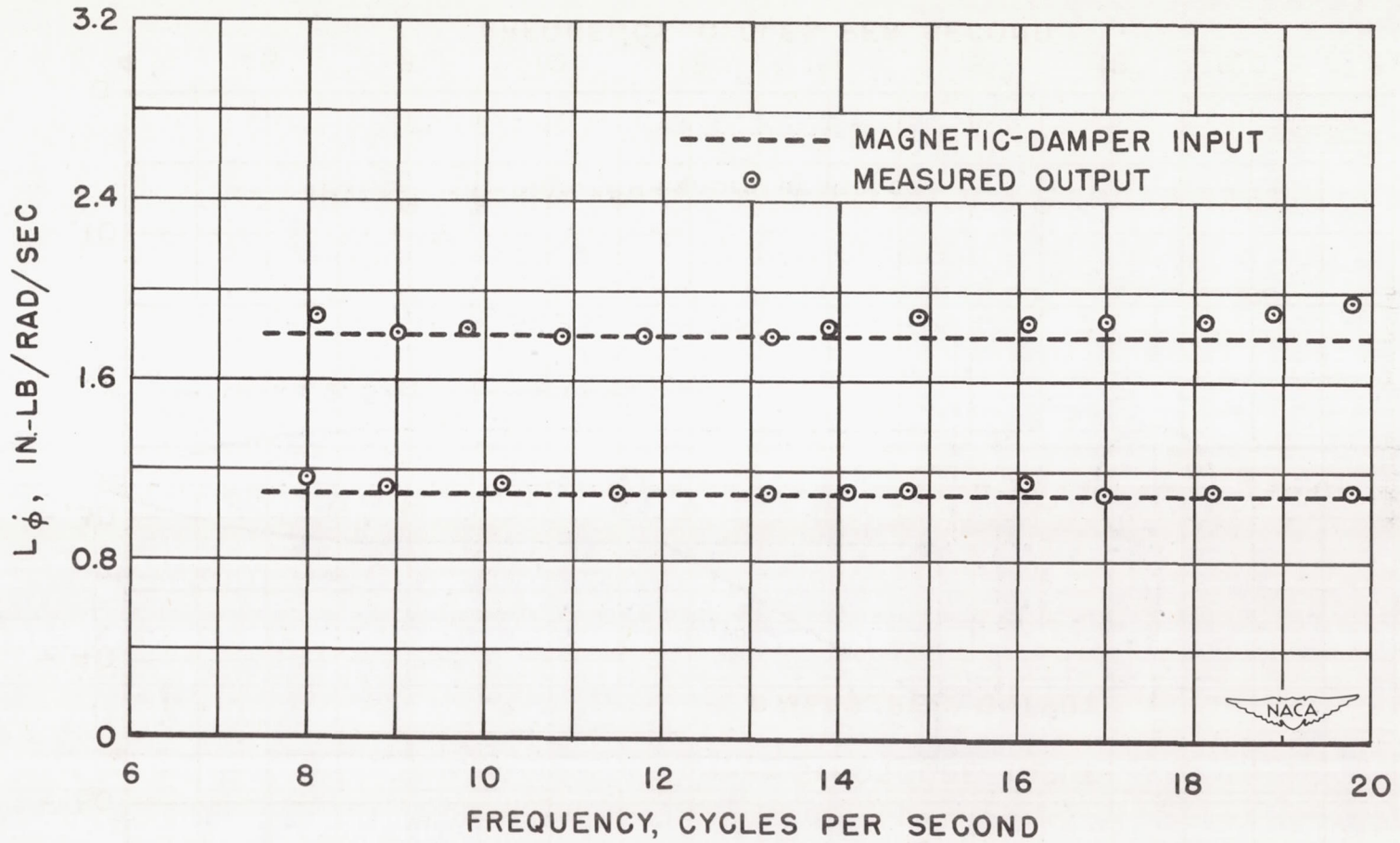
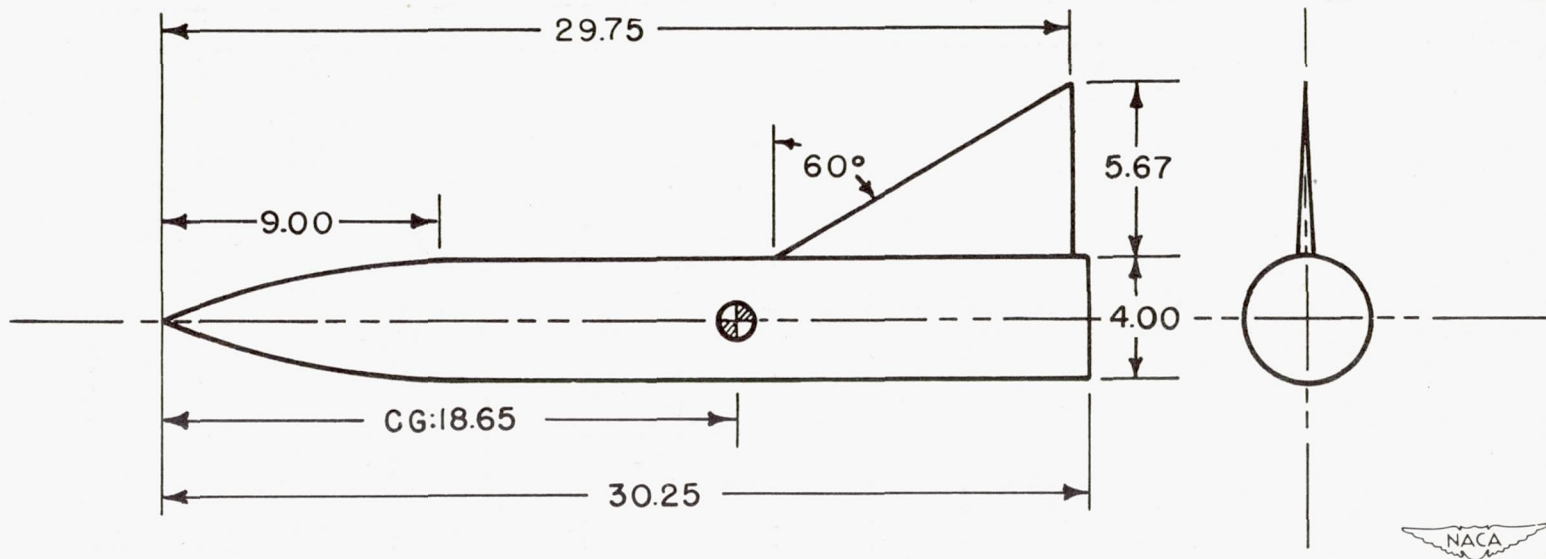


Figure 6.- Comparison of magnetic-damper input and measured output of the simulated aerodynamic damping-in-roll derivative $L\dot{\phi}$.



NOTE: All dimensions are in inches

Figure 7.- Model used for wind-tunnel tests.

NACA

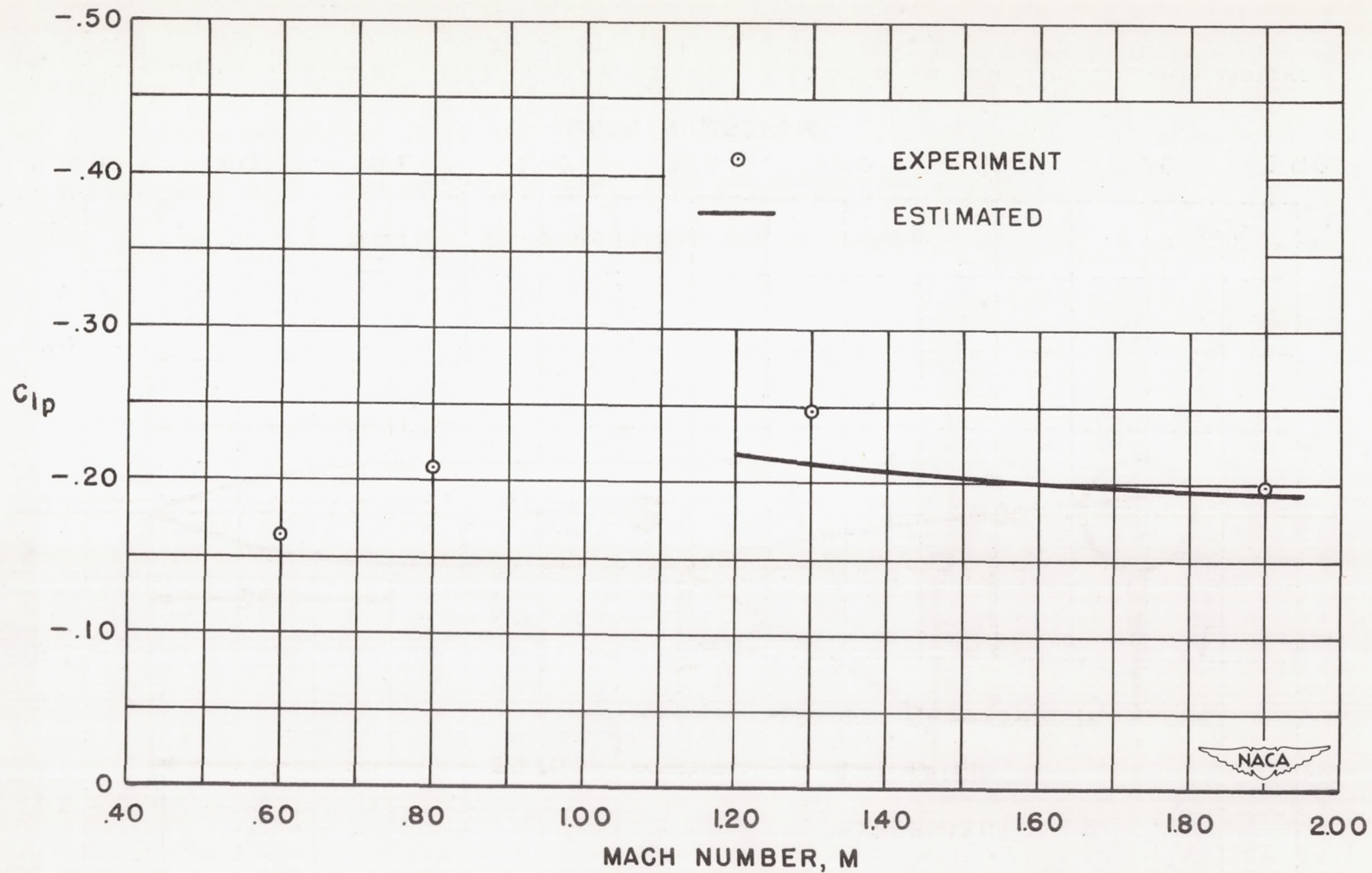


Figure 8.- Variation with Mach number of experimental and estimated values of damping-in-roll coefficient, C_{lp} .

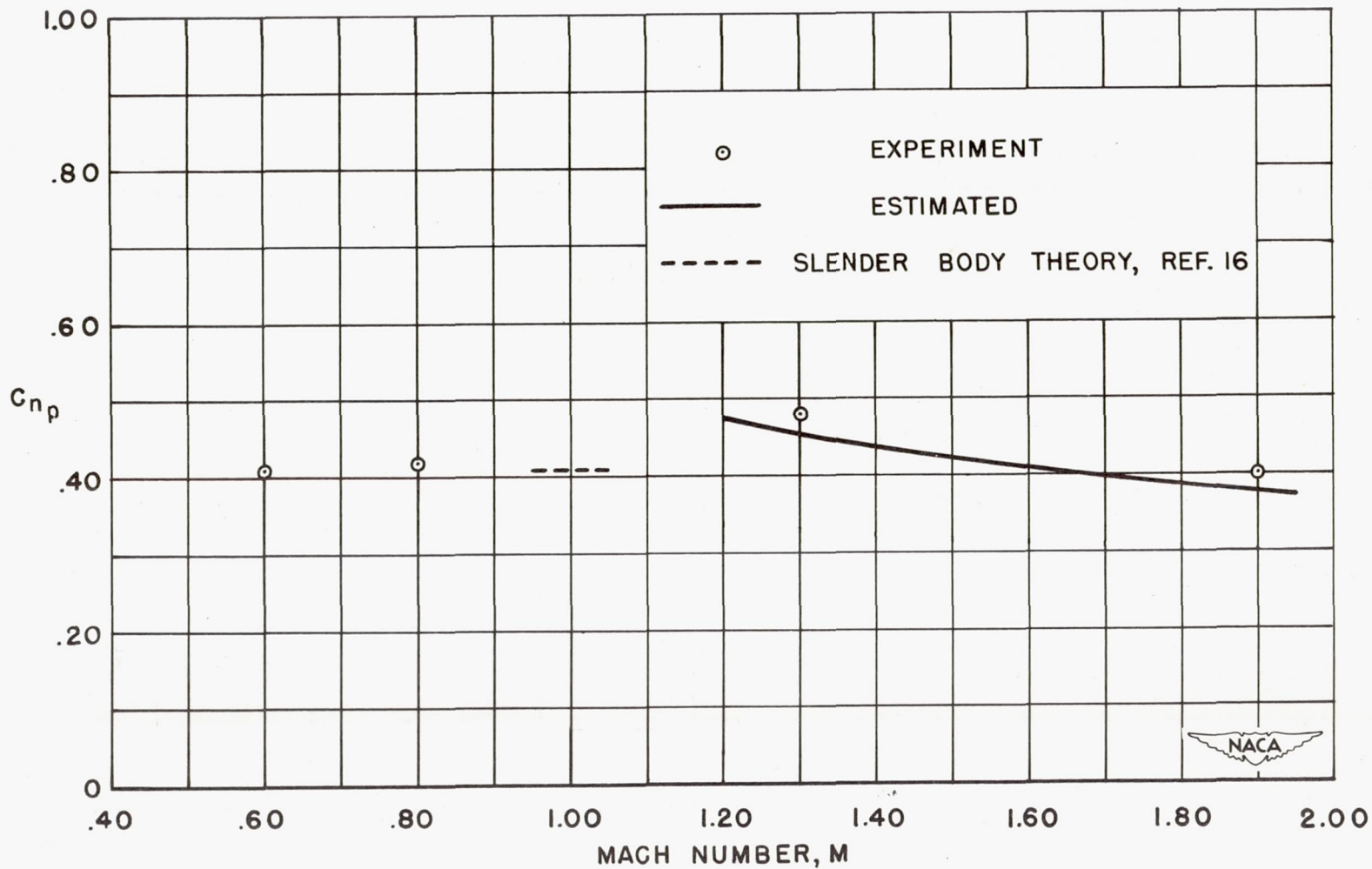


Figure 9.- Variation with Mach number of experimental and estimated values of cross-derivative coefficient, C_{np} .

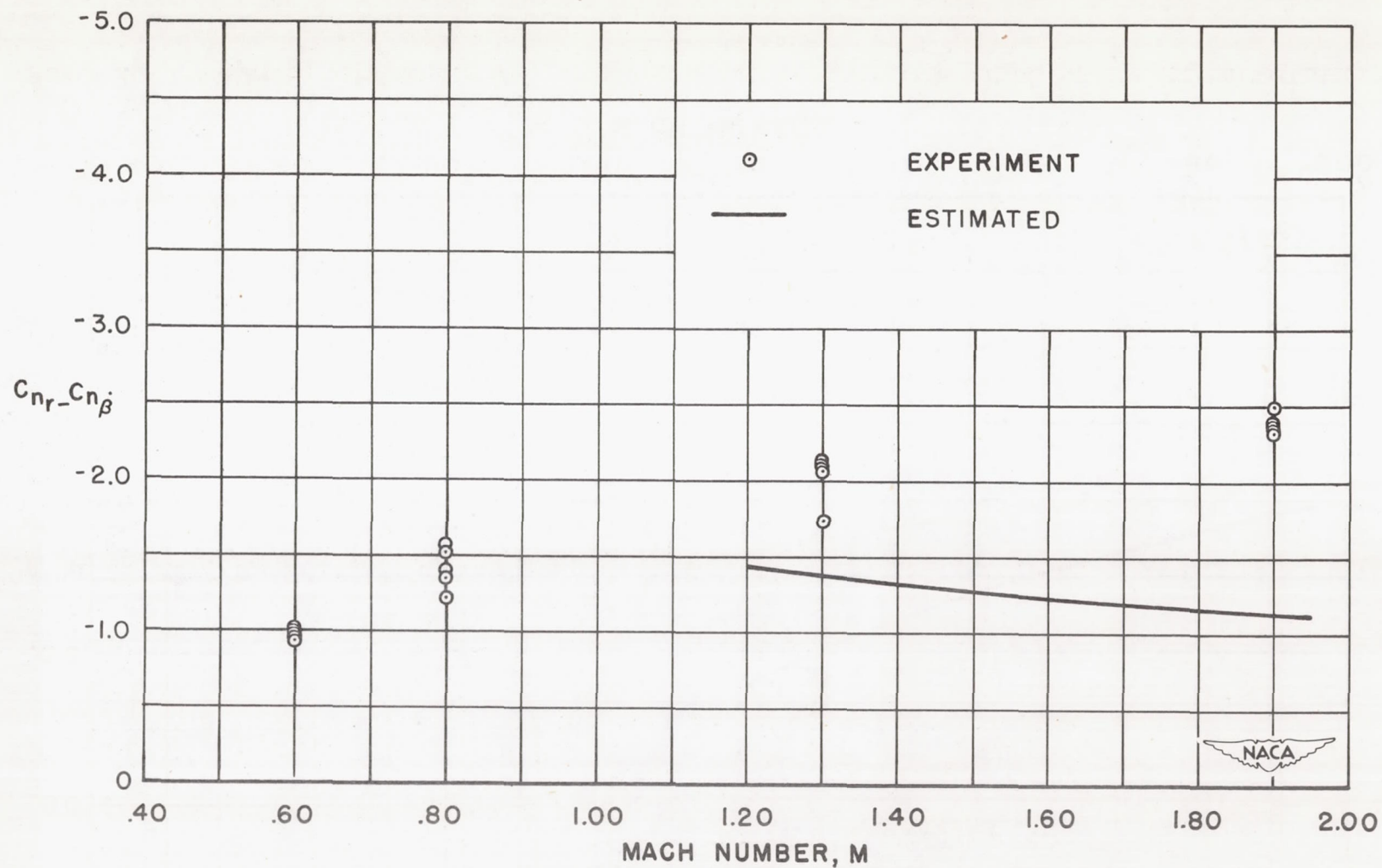


Figure 10.- Variation with Mach number of experimental and estimated values of damping-in-yaw coefficient, $C_{nr} - C_{n\dot{\beta}}$.

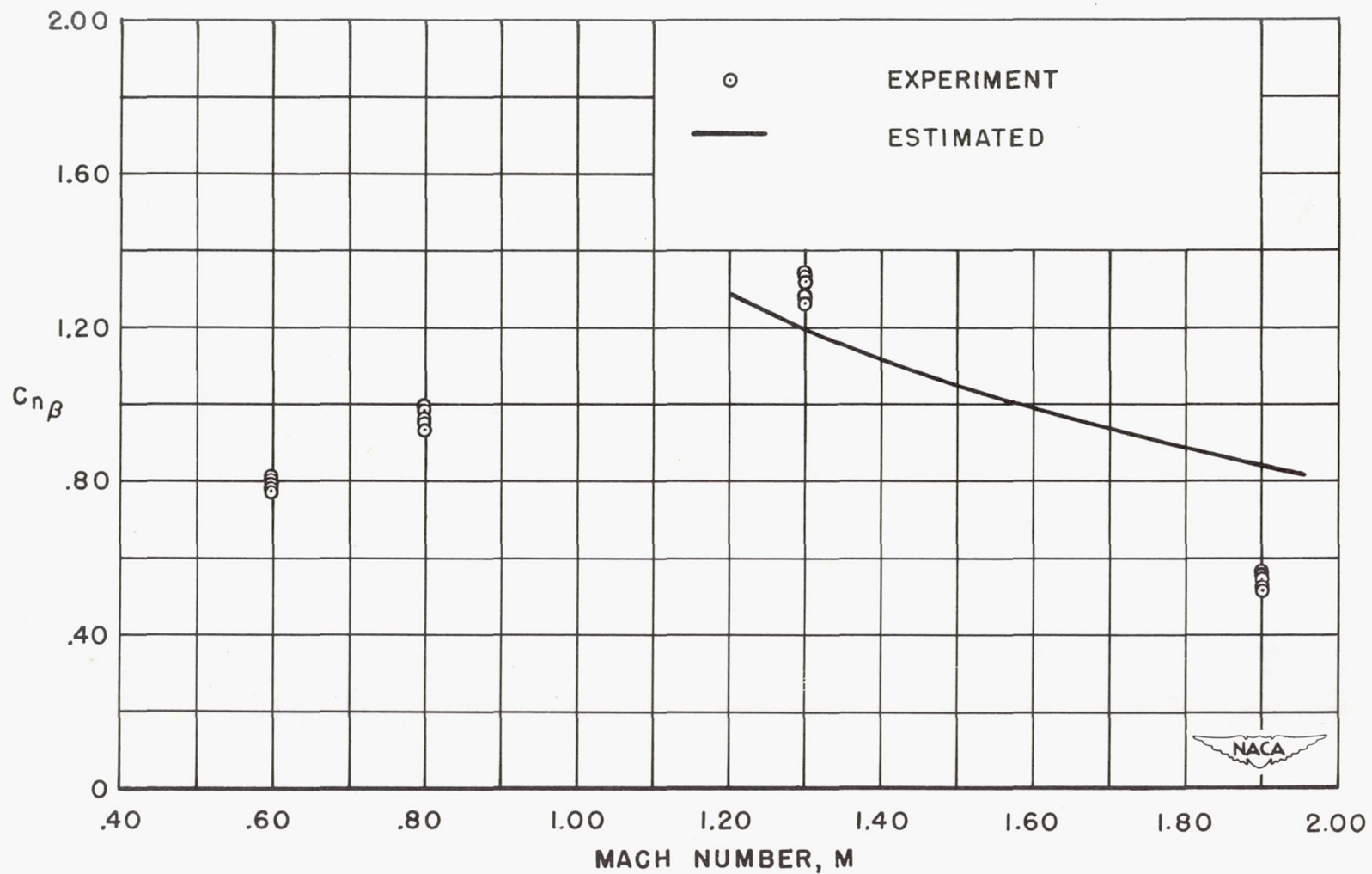


Figure 11.- Variation with Mach number of experimental and estimated values of directional stability coefficient, $C_{n\beta}$.